



# Experimental Analysis of Short-Circuit Scenarios Applied to Silicon-Graphite/Nickel-Rich Lithium-Ion Batteries

J. Sturm,<sup>1,\*,z</sup> S. Friedrich,<sup>1,\*</sup> S. Genies,<sup>2</sup> D. Buzon,<sup>2</sup> Rahn-Koltermann G.,<sup>1</sup>  
A. Rheinfeld,<sup>1</sup> and Jossen A.<sup>1,3</sup>

<sup>1</sup>Institute for Electrical Energy Storage Technology (EES), Technical University of Munich (TUM), Arcisstr. 21, 80333 Munich, Germany

<sup>2</sup>Univ. Grenoble Alpes, CEA, Liten, DEHT, 38000 Grenoble, France

<sup>3</sup>Munich School of Engineering (MSE), Technical University of Munich (TUM), Lichtenbergstr. 4a, 85748 Garching, Germany

Short-circuit incidents pose a severe safety threat to lithium-ion batteries during lifetime. Understanding the underlying electrochemical behavior can help to mitigate safety risks. The electrochemically-caused rate-limiting behavior is analyzed using a quasi-isothermal test-bench, where external and local short-circuit conditions are applied to single-layered pouch cells (<50 mAh). The cell voltage, the heat generation rate, and either the short-circuit current or a local electrical potential are measured and used to characterize the short-circuit intensity. The results of 35 custom-built silicon-graphite SiC/NCA and SiC/NMC-811 cells with 2.5 wt.-% silicon are benchmarked to previously studied graphite G/NMC-111 cells. An additional current plateau appears for the silicon-graphite/nickel-rich cells, which is ascribed to the anode-limited electrode balancing. At a maximum, 29% of the total dissipated heat is caused during over-discharge. The effect of cyclic aging on the impact of the short-circuit behavior is investigated with aged single-layered pouch cells (SoH < 80%), which revealed nearly the same levels of over-discharge as non-aged cells. A lithium reference electrode is used to visualize polarization effects in the anode during ESCs and to evaluate the onset of copper dissolution (>3.2 V vs Li/Li<sup>+</sup>), which could be estimated up to 20% of the negative current collector mass.

© 2022 The Author(s). Published on behalf of The Electrochemical Society by IOP Publishing Limited. This is an open access article distributed under the terms of the Creative Commons Attribution 4.0 License (CC BY, <http://creativecommons.org/licenses/by/4.0/>), which permits unrestricted reuse of the work in any medium, provided the original work is properly cited. [DOI: 10.1149/1945-7111/ac51f3]



Manuscript submitted November 14, 2021; revised manuscript received January 18, 2022. Published February 28, 2022.

Supplementary material for this article is available [online](#)

Crucial safety incidents in lithium-ion batteries (LIBs) are often triggered via internal (ISC) or external (ESC) short-circuits. Between the years 2014 and 2019, 78% of all fire incidents with electric vehicles (EVs) revealed either an ISC, ESC, or both events.<sup>1</sup> Consequently LIB safety is significantly correlated to the short-circuit behavior of the single cell, which can trigger a thermal runaway event and initiate thermal propagation to other cells within a battery module or even to the entire battery pack in an EV.<sup>2</sup> Understanding the short-circuit behavior of LIBs can help to develop mitigation strategies either for the event itself via advanced cell and electrode design<sup>2-4</sup> or its critical consequences, such as thermal overheating<sup>5</sup> and possible thermal runaway events. Short-circuit test procedures reveal a variety of events in laboratory conditions to emulate and investigate short-circuits, as they appear in the field.<sup>6</sup>

Mechanical deformation is most commonly used beside nail penetration to emulate field-like ISCs, which trigger a short-circuit close to or in the penetrated spot via electrically contacting the single electrode/current collector layers in the electrode stack of the cell.<sup>7</sup> Alternatively, ISCs can be triggered without any external event<sup>8</sup> by inserting local defects in the electrode stack.<sup>9</sup> Beside mechanical triggers, over-heating<sup>10</sup> and over-charge or -discharge,<sup>11</sup> can initiate ISCs via exceeding the cell's safe operating range and the related malfunction of components such as separator melting.

ESCs are realized via an electrical contact between the cell terminals. The electrical resistance of the contact determines the intensity of the short-circuit event to a so-called "hard short-circuit" (i.e. low-ohmic resistance) or a so-called "soft short-circuit" (i.e. high-ohmic resistance).<sup>2</sup> ESC procedures reveal higher reproducibility than ISC tests<sup>12</sup> due to the repeatable test condition in form of an external resistance in the external circuit and the same current pathway via the tabs and current collectors to the electrode stack.

In this work, the short-circuit behavior of small, laboratory pouch-type cells is analyzed in order to better understand the

electrochemically-caused current, terminal voltage, and heat generation rate limiting behavior to derive cell designs with improved intrinsic safety of LIBs.<sup>2</sup> In order to evaluate a cell's intrinsic safety when it comes to field-like short circuit conditions, controllable and reproducible short-circuit triggers are required. For this reason, overheating, over-charge, and over-discharge<sup>11</sup> are discarded as possible short-circuit triggers, as the imposed short-circuit trigger cannot be considered as predictable or reproducible for most use cases. A variety of relevant ESC and ISC testing procedures on single cell level are summarized in Table I.

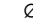




To emulate ISCs, current research aims to improve the reproducibility of nail penetration testing<sup>13</sup> and to develop instrumented penetration devices<sup>21</sup> incorporating sensors to measure the local temperature increase and the electrical potential drop. Nail penetration testing is characterized via the diameter  $d$  of the used device, its tip condition (i.e. cone angle  $\alpha$ ), penetration speed ( $v$ ), penetration depth ( $s$ ), and electrical conductivity ( $C$ ) or non-conductivity ( $NC$ ).<sup>13</sup> Tests with electrically conductive nails reveal poor reproducibility<sup>19</sup> caused by the varying contact condition in the penetration spot.<sup>7</sup> The altering electrical resistance between nail, electrodes, and current collectors determines the current flow through the penetration spot and cannot be controlled during the event.<sup>19</sup> Moreover, the separator properties such as mechanical puncture resistance and thermal melting resistance<sup>11</sup> can significantly affect the event.


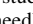
As shown in our previous work,<sup>12</sup> the correlation of the measured electrical and thermal behavior combined with multidimensional-multiphysics simulation studies helps to better analyze and understand the observed short-circuit behavior and mitigate the impact of the test conditions. Therefore, the most reproducible nail penetration technique ( $d = 1\text{ mm}$ )<sup>12</sup> embedded in the quasi-isothermal test bench is used in this work to emulate ISC events. The investigated nail penetration tests of this work are similarly called local short-circuit (LSC) tests. As the focus of this work lies on the electrode level and due to the quasi-isothermal test bench, possible non-uniform utilization of the active material or inhomogeneous temperature distribution during the thermal runaway in commercial cells cannot

\*Equal Contribution.

<sup>z</sup>E-mail: [johannes.sturm@tum.de](mailto:johannes.sturm@tum.de)

Table I. Literature review of short-circuit analysis of lithium-ion batteries on single cell level with defined initiation points.

ISC	ESC	Measurement	Analysis	Chemistry	Capacity	TR	Format	Sim	Ex	References
✓		Ⓢ Ⓣ io- 	$\varnothing_{C,\alpha}^v$	G/LCO	20–820 mAh	✓	PB		✓	Yokoshima et al. 2019
✓		Ⓢ Ⓣ Ⓟ	$\varnothing_{C,NC,\alpha}^{v,s}$ , IM, $\infty$ , Gas, 	G/LNCO-LCO	5.5 Ah	✓	PB		✓	13
✓		Ⓢ Ⓣ	$\varnothing_C^v$ , PCM	G/LMO	5.25 Ah	✓	PM	✓	✓	14
✓		Ⓢ Ⓣ	SMA, $\varnothing_C^v$	n.a./NMC	1 Ah	✓	PB		✓	9
✓		Ⓢ Ⓣ	$\varnothing_{wax}$ , PCM	G/NCA	2.4 Ah	✓	CY	✓	✓	15
✓		Ⓢ Ⓣ Ⓡ	$\varnothing_C^v$ , 	n.a.	20 mAh–3 Ah	✓	PB		✓	16
✓		Ⓢ Ⓣ Ⓡ	$R_c$ , SoC, PCM	G/LCO	n.a.	✓	PB	✓	✓	17
✓	✓	Ⓢ Ⓣ	$d_E$ , $\varnothing_C$ , $R_{ext}$ , P °C, PCM	n.a./LCO	0.65–5 Ah	✓	PB	✓	✓	18
✓	✓	Ⓢ Ⓣ Ⓡ	$\varnothing_C$ , $R_{ext}$ , PCM	G/NMC-111	<60 mAh		PB	✓	✓	12
✓	✓	Ⓢ Ⓣ	$d_{sep}$ , $\varnothing_C^s$ , SoC, $R_{ext}$	G/LCO	3.6–4.2 Ah	✓	PB		✓	11
✓	✓	Ⓢ Ⓣ Ⓡ	$\varnothing_{C,NC,\alpha}^{v,s}$ , $R_{ext}$	G/LMO-NMC	15 Ah	✓	PB		✓	19
	✓	Ⓢ Ⓣ Ⓡ	$d_E$ , SoC, $T_0$ , $R_{ext}$ , TD, PCM, 	G/NMC-111	19–68 mAh		PB	✓	✓	3, 4
	✓	Ⓢ Ⓣ Ⓡ	PCM, P °C	G/NMC-111	3–27 Ah	✓	PB/PM/CY	✓		5
	✓	Ⓢ Ⓣ Ⓡ IR	$R_{ext}$ , mechanical constraint, 	G/NMC-111	4.5 mAh–	✓	Coin	✓	✓	6
	✓	Ⓢ Ⓣ Ⓡ	SoC, $T_0$ , $R_{ext}$	G/NCA	10 Ah		PB			
		Ⓢ Ⓣ Ⓡ		n.a./NMC	2 Ah		CY	✓	✓	20

**Note.** TR thermal runaway Sim simulation study Ex experimental study Ⓢ Voltage measurement/V Ⓣ Temperature measurement/K Ⓟ Pressure measurement/MPa Ⓡ Current measurement/A io- in-operando X-ray analysis IR in-operando infrared analysis  $\varnothing$  needle diameter/m C,NC electrically conductive/non-conductive  $\alpha$  angle of penetration device/rad  $v$  penetration speed/m s<sup>-1</sup>  $s$  penetration depth/m IM insulation material  $\infty$  under air or N-atmosphere Gas gas analysis  post-mortem X-ray analysis PCM physicochemical model SMA shape memory alloy  $R_c$  contact resistance in penetration site/ $\Omega$  SoC state of charge  $d_E$  electrode thickness/m  $R_{ext}$  external ohmic resistance/ $\Omega$  P °C cooling condition  $d_{sep}$  separator thickness/m  $T_0$  initial temperature/K TD tab design PB pouchbag format PM prismatic format CY cylindrical format.

be investigated with our approach. Similar to our previous work,<sup>12</sup> other works used an electrically contacted nail with an additional temperature sensor within the tip of the nail,<sup>14</sup> which enables to measure both the electrical potential and temperature at the penetration spot.

Besides, X-ray analysis is a more advanced but also more expensive method to correlate the cell's electrical behavior to its thermal behavior,<sup>22</sup> which uses the cell's terminal voltage and in situ images of the cell during the short-circuit event. Moreover, LSCs can also be triggered in situ at elevated temperatures, as an alternative to the widely used mechanical nail penetration. For example, shape-memory alloys embedded in the electrode stack bend up at higher temperatures and penetrate the separator, shorting anode and cathode.<sup>9</sup> Also wax-based internal short-circuit devices<sup>15,23</sup> may be used, whereby the melting-point of the embedded wax determines the onset of the short-circuit event after a heat-up phase. Nevertheless, inserting triggers within individual cells most likely alters the electrical, thermal, and mechanical behavior of the cell during initiation and the impact of this modification is complex to be determined, which is why these methods are neglected within this work. Most works dealing with emulating ISCs are of experimental nature, as simulating thermal side reactions possibly leading to a thermal runaway (TR)<sup>14</sup> is to date still rather complex and challenging.

The impact of cell's capacity, SoC, internal resistance, and effect of the ambient temperature on a cell's short circuit behavior is frequently investigated in literature.<sup>12,20</sup> The cell chemistry itself is assumed to have a lower influence on the intensity of the short-circuit than the design of the electrode stack,<sup>3,4</sup> the electrode's surface,<sup>6</sup> used external resistances  $R_{\text{ext}}$ ,<sup>3,6</sup> and especially the specific capacity of the electrodes.<sup>6</sup> For this reason, both the ESC and LSC behavior of high capacity silicon-graphite/nickel-rich chemistries are investigated in this work and compared to graphite/NMC-111 cells, which has not been reported in literature so far. ESC testing procedures as described in our previously presented quasi-isothermal test bench<sup>3,4,12</sup> are used in this work to emulate short-circuits of different intensities serving as reproducible,<sup>6,12</sup> validated benchmark for LSC tests and the additional remaining short-circuit tests focusing on aged single-layered pouch (SLP) cells and SLP cells with a reference electrode setup.

Also other works<sup>11,18,19,24</sup> compare, correlate, and investigate both different ESC and LSC scenarios as in this work. Zhao et al.<sup>18</sup> correlate both events by testing 0.65 A h to 5 A h LIBs and explain the different short-circuit behavior with the varying capacity of the tested cells. As a result, ESCs applied to low-capacity cells reveal higher-ohmic short-circuit behavior due to the higher internal resistance and the chance of malfunction of the LSC tests is higher for high-capacity cells.<sup>18</sup> In the work of Abaza et al.,<sup>19</sup> electrical and thermal characteristics from ESC and LSC tests with 15 A h LIBs are used to estimate the short-circuit resistance. Although the current flow and electrical potentials across the active electrode area are significantly different<sup>12</sup> during the investigated ESC and the LSC tests, the short-circuit resistance is estimated via the measured terminal voltages with a reconstructed current profile of the LSC test (i.e. nail penetration), which is gained by correlating the LSC measurement results to the ESC results.

To conclude, to the best of our knowledge, there is no comparable research on the short-circuit behavior of high-capacity silicon-graphite/nickel-rich chemistries in LIBs, where the terminal voltage, the heat generation rate, and either the short-circuit current or local electrical potentials across the active electrode area can be compared for ESC and LSC events.

### Scope and Aims of the Experimental Study

In this work, ESC (i.e. external condition of  $0 \text{ V} \approx R_{\text{ext}} = 0 \text{ m}\Omega$ ,  $50 \text{ m}\Omega$ ,  $250 \text{ m}\Omega$ , and  $500 \text{ m}\Omega$ ) and LSC (i.e. penetration with  $\varnothing 1 \text{ mm}$  needle) tests are applied to single-layered pouch-type LIBs using a quasi-isothermal calorimetric test bench.<sup>3</sup> Characteristics of

the cells' short-circuit behavior are analyzed from measurement data, such as discharge current flow  $I_{\text{sc}}$ , terminal voltage  $E_{\text{sc}}$ , heat generation rate  $\dot{Q}_{\text{tot}}$ , dissipated heat  $Q_{\text{tot}}$ , and locally measured electrical potentials  $\Phi_{\text{sc}}$ .

In extension to our previous works,<sup>2,3,12</sup> we focus in this work on silicon-graphite/nickel-rich cell chemistries instead of graphite/NMC-111 to extend our studies on state-of-the-art high energy LIBs.<sup>24</sup> The tested SiC/NCA and SiC/NMC-811 SLP cells are designed with an anode-limited electrode balancing<sup>24</sup> instead of the former investigated cathode-limited SLP cells.<sup>2,3,12</sup> This tested cell balancing is based on previously characterized commercial high-energy cells.<sup>24</sup> However, the anode is still assumed to be limiting during over-discharge, whereas our cells with over-dimensioned cathode capacities are supposed to be preferably free from cathode limitations.

Results of G/NMC-111 from our previous work<sup>12</sup> are used as a reference. To simplify the nomenclature, the single-coated, single-layered pouch cells of G/NMC-111, SiC/NCA, and SiC/NMC-811 are referenced as NMC-111, NCA, and NMC-811, respectively. Cyclic aging and subsequent ESC tests are applied to NCA and NMC-811 SLP cells to analyze the impact of increased impedance and SoH levels below 80% on the cells' short-circuit behavior. Within the self-built SLP cells, reference electrode setups were inserted within the cells to estimate the anode's polarization/potential state during the short-circuit event. Therefore, the electrical potential between the cell's negative current collector tab and a lithium metal reference electrode is measured as well. This additional measurement signal helps to better understand the over-discharge effect and the related copper dissolution from the negative current collector during the late stages of the applied short-circuit events, which is visualized and analyzed in the post-mortem part of this work.

## Experimental

**Coin and SLP Cell Manufacturing.**—All electrodes were dried under vacuum at  $90 \text{ }^\circ\text{C}$  (B-580, Büchi, Switzerland) for at least 10 h before assembly. Similarly, separator, pouch-foils, and current collectors were dried in an oven at  $60 \text{ }^\circ\text{C}$  for at least 15 h. In general, both coin and SLP cells were assembled under argon atmosphere in a glove box ( $\text{H}_2\text{O}$ ,  $\text{O}_2 < 0.1 \text{ ppm}$ , MBraun, Germany).

**2032-type coin cell setup.**—The half cells incorporated pristine SiC (88  $\mu\text{m}$ , 45.8% porosity), NCA (99  $\mu\text{m}$ , 50.5% porosity), or NMC-811 (73  $\mu\text{m}$ , 42.4% porosity) with  $\varnothing 14 \text{ mm}$  (Custom Cells, Germany) vs lithium metal ( $\varnothing 15.6 \text{ mm} \times 130 \mu\text{m}$ , MTI Corporation, USA) with a standard polyolefin separator (41% porosity,  $\varnothing 16 \text{ mm} \times 25 \mu\text{m}$ , Celgard, USA). More specifications of the anode and the cathode composites, the separator, and the NMC-111 SLP cells<sup>3,4,12</sup> as benchmarks are shown in Table II. 2032-type housing kits including top and bottom can as well as the insulation ring, two types of spacers (thickness of 0.5 mm and 1 mm) made of stainless-steel were used together with a radial spring for the coin cell setup. The coin cells were filled with  $120 \mu\text{l}$  and  $100 \mu\text{l}$ <sup>25</sup> of 1 M  $\text{LiPF}_6$  in EC:DMC:EMC 1:1:1 (by volume)<sup>26</sup> (Solvionic, France) for the anode and the cathode samples. Similar to our previous work, the NMC-811 half cells were only functional if the pristine cathode samples were filled with electrolyte under low-pressure conditions in a vacuum sealer.<sup>25</sup>

**Counter-tab, single-layered pouch (SLP) cell setups.**—Cells with an anode/separator/cathode stacking sequence are only used with counter-tab design. The geometrical sizes of electrodes, separator, the pouchbag foil, and the entire SLP cell setup are signed for the NCA and the NMC-811 cells similarly to the NMC-111 cells.<sup>3,4,12</sup> NMC-111 cells consisted of one outer wrapping of separator (i.e. separator/anode/separator/cathode/separator). A scheme of the standard SLP cell setup with geometrical sizes is shown in Fig. 1. Note, that Fig. 1 shows the open SLP cells before the filling and sealing

**Table II. Single-layered pouch (SLP) cell design for NCA, NMC-811, and the previously studied NMC-111 cells.<sup>24</sup>**

Description	Unit	Negative electrode	Separator <sup>IV</sup>	Positive electrode
<b>NCA SLP cells</b>				
Active material <sup>a)</sup>	—	Graphite + Silicon (2.5 wt.-%)	—	NCA
Specific capacity <sup>d),c)</sup>	mAh g <sup>-1</sup>	460.1	—	168.2
Active material content <sup>a)</sup>	wt.-%	88	—	90
Thickness <sup>a),b)</sup>	μm	88	25	99
Porosity <sup>a)</sup>	vol.-%	45.8	41	50.5
Areal capacity <sup>d),c)</sup>	mAh cm <sup>-2</sup>	3.37	—	3.48
Electrolyte <sup>a)</sup>	—	1 M LiPF <sub>6</sub> in EC:DMC:EMC 1:1:1 (by volume)		
<b>NMC-811 SLP cells</b>				
Active material <sup>a)</sup>	—	Graphite + Silicon (2.5 wt.-%)	—	NMC-811
Specific capacity <sup>d),c)</sup>	mAh g <sup>-1</sup>	460.1	—	216.4
Active material content <sup>a)</sup>	wt.-%	88	—	90
Thickness <sup>a),b)</sup>	μm	88	25	73
Porosity <sup>a)</sup>	vol.-%	45.8	41	42.4
Areal capacity <sup>d),c)</sup>	mAh cm <sup>-2</sup>	3.37	—	3.63
Electrolyte <sup>a)</sup>	—	1 M LiPF <sub>6</sub> in EC:DMC:EMC 1:1:1 (by volume)		
<b>Benchmark: NMC-111 SLP cells</b>				
Active material <sup>a)</sup>	—	Graphite	—	NMC-111
Specific capacity <sup>4</sup>	mAh g <sup>-1</sup>	357.3	—	157.4
Active material content <sup>a)</sup>	wt.-%	96	—	86
Thickness <sup>a),3,4,27</sup>	μm	67	25	79
Porosity <sup>a),4,27</sup>	vol.-%	51.3	41	48.7
Areal capacity <sup>4</sup>	mAh cm <sup>-2</sup>	2.4	—	2.2
Electrolyte <sup>a)</sup>	—	1 M LiPF <sub>6</sub> in EC:DMC 1:1 (by volume) with 2 wt.-% VC		

a) Supplier's information. b) Measured with 49–56 digital micrometer, TMI, USA. c) Capacity measured with half cells vs lithium metal at 0.02C CC discharge (i.e. delithiation). d) Calculated from weight measurement with MX5 (accuracy of 1 μg), Mettler-Toledo, USA, and the densities of copper (8.96 g cm<sup>-3</sup>) and aluminum (2.7 g cm<sup>-3</sup>).

process, which is why the pouchbag foil is not folded in the depicted schematic view. The specific capacity of the SiC composite (2.5 wt.-% Si) is measured in coin cells to a value of around 460 mAh g<sup>-1</sup>, which results in a lower areal capacity of 3.37 mAh cm<sup>-2</sup> compared to the nickel-rich cathodes. The NCA composite with 3.48 mAh cm<sup>-2</sup> and 168 mAh g<sub>NCA</sub><sup>-1</sup> reveals a 4% lower measured areal capacity than the NMC-811 composite with 3.63 mAh cm<sup>-2</sup> and 216 mAh g<sub>NMC-811</sub><sup>-1</sup>. Both SLP cells with and without reference electrodes were filled with 520 μl 1 M LiPF<sub>6</sub> in EC:DMC:EMC 1:1:1 (by volume). Applying Faraday's law and assuming an electrolyte reference concentration of 1 mol l<sup>-1</sup>, the lithium-ions in the electrolyte could provide maximally a charge of 13.94 mAh.

In this work, the oversized cathode areal loadings are chosen to gain an anode-limited electrode balancing in the custom-built SLP cells. In the context of this work, anode-limiting means that the anode capacity is smaller than the cathode capacity, leading to a capacitively oversized cathode. The porosity of electrodes and separator are in a comparable order of magnitude for the NCA, NMC-811, and NMC-111 cells. The coating thickness of the graphite composite is around 24% smaller than the SiC composite. The NCA composite thickness is about 36% and 25% larger than the NMC-811 and NMC-111 composite due to its slightly increased porosity. The NMC-111 cells provide approximately 63% and 60% areal capacity of the NCA and NMC-811 cells.

The thickness of the positive aluminum current collector was measured for all three SLP cells to be 20 μm. The thickness of the copper current collector foil was measured to be 14 μm for the NCA and NMC-811 cells and to be 18 μm for the NMC-111 benchmark cells. The same current collector tabs in counter-tab design were used for NCA and NMC-811 as for the NMC-111 cells. Three ultrasonic welding spots joined the current collector foil electrically to the current collector tabs, as illustrated in Fig. 1. The used counter-tab design minimizes the impact of the tab pattern on the electrical potential variance across the active electrode area.<sup>3,24</sup> All SLP cells were manually manufactured and the stacked layers were

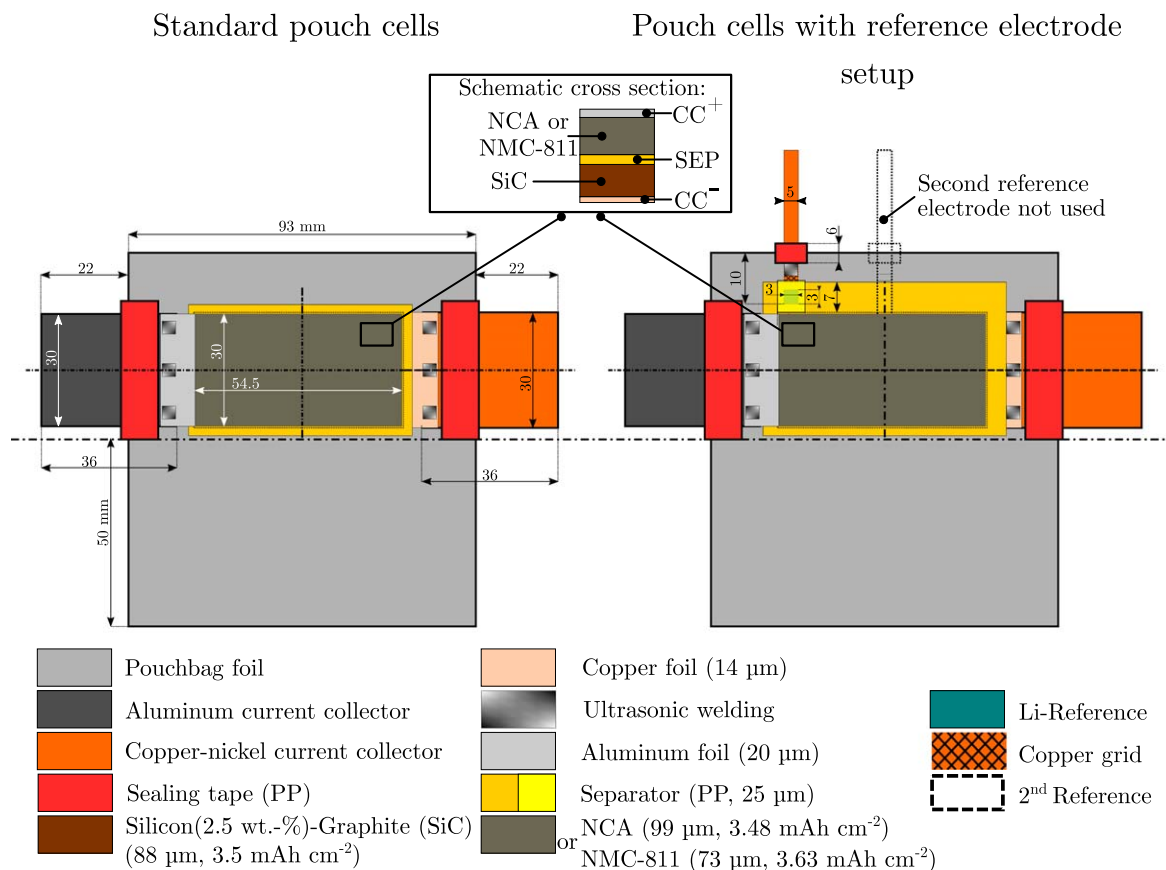
fixed each with polyester or polyimide tapes (MTI Corporation, USA). The used electrolyte<sup>26</sup> for the NCA and NMC-811 cells was chosen according to characterization results of state-of-the-art high-energy LIBs.<sup>25,27</sup> The manufactured NCA and NMC-811 SLP cells are filled with 520 μl of the electrolyte and sealed under argon atmosphere prior to an evacuation process of the dry electrode stack (i.e. chamber pressure  $p_{\min} < 100$  mbar).

The standard SLP cells incorporated only the anode/separator/cathode stack embedded in the pouchfoil and electrically-connected via the counter-tab current collectors. A second SLP cell setup with reference electrodes was used as shown in Fig. 1 on the right side. Within this work, we focus on the lithium metal reference electrode, which was incorporated as shown in Fig. 1 next to the electrode stack on the left top of the separator sheet and covered with an additional small-sized sheet of separator. The lithium metal electrode (3 mm × 3 mm × 130 μm, MTI Corporation, USA) was applied into a copper grid (CEA, France), which was electrically contacted via ultrasonic welding to a copper/nickel tab for connection to the potentiostat.

The manufactured SLP cells with reference electrode setup additionally included a second reference electrode in the center of the electrode stack in between the separator and the cathode, which was electrically insulated with an additional small-sized layer of separator toward the cathode. In this work, we do not present results gained from the second reference electrode, as this is content of future work and was out of scope for this work. Nevertheless, OCV, DVA, electrochemical impedance spectroscopy (EIS) characterization tests, and the short-circuit results are analyzed within this work, which suggests a negligible influence of the second reference electrode on the presented results of this work.

The practical areal capacity for the NMC-111, NCA, and NMC-811 SLP cells can be calculated to 1.5 mAh cm<sup>-2</sup>,<sup>12</sup> 2.6 mAh cm<sup>-2</sup>, and 2.3 mAh cm<sup>-2</sup>. These values are calculated with the capacity gained from the capacity check-up according to Table III after formation (see Table IV) and the active electrode area ( $A_{\text{act}} = 16.4$  cm<sup>2</sup>). In this work, the NMC-111#5 and #7 of the





**Figure 1.** Schematic view of the self-built NCA and NMC-811 SLP cells in the standard configuration (left) and the reference electrode setup (right). The view shows the unfolded, open pouchbag foil setup with the layered electrode stack right before the filling and sealing process. Only the most important geometrical sizes are depicted together with the description of the most relevant components. Results from the second reference electrode in the middle of the cells are out of scope for this work.

single layer design (i.e. P1<sup>12</sup>) are used as benchmarks for the 0 V and 500 m $\Omega$  ESC cases. The capacities accounted for 23.3 mAh and 26.9 mAh and the 1 kHz impedance was measured to 347 m $\Omega$  and 301 m $\Omega$ , respectively.

The short-circuit behavior of NCA and NMC-811 cells is analyzed and compared to studied NMC-111<sup>12</sup> cells, showing a similar electrode and cell design, and a comparable set of incorporated chemistries, i.e. graphite-type anodes and transition-metal-oxide-type cathodes.

**Test protocols for coin and SLP cells.**—After 8 h resting time to guarantee sufficient soaking of the coin cells, a similar formation protocol as applied to the SLP cells (see Table X in the appendix) is conducted excluding the EIS test. Next, three OCV cycles (i.e. CC<sub>CH</sub>-CC<sub>DCH</sub> at 25 °C) were conducted with a current rate of 0.02C between 3 V and 4.3 V for the cathode and between 10 mV and 1.5 V for the anode coin cells. The 3<sup>rd</sup> OCV cycle is used for the DVA of the SLP cells and for the mean measured areal capacity. The results are summarized in Table II.

The formation procedure for the SLP cells is based on the electrode supplier recommendation (Custom cells, Germany) and shown in Table X in the appendix. The resting time after cell assembly and filling was kept short (<20 min) to exclude possible copper dissolution from the negative current collector. Optional OCV and/or EIS characterization protocols are applied to chosen NCA and NMC-811 SLP cells to compare cell setups with and without reference electrodes.

The OCV test for the SLP cells incorporated a CC<sub>DCH</sub>-CC<sub>CH</sub>-CC<sub>DCH</sub> at 0.02C and 25 °C. The procedure of the DVA using the OCV data of coin/half and SLP/full cells has already

been explained in detail in our previous works<sup>12,24,25</sup> and is not further detailed here. The results of the DVA are depicted in the supplementary part of this work (available online at [stacks.iop.org/JES/169/020569/mmedia](https://stacks.iop.org/JES/169/020569/mmedia)). As a result, the electrode balancing for the NCA and NMC-811 cells is anode-limited. For the studied short-circuit events, the cathode's overdimensioning in terms of capacity becomes relevant after the cell is fully discharged (i.e. SoC < 0%) as it majorly affects the electrochemically-caused rate limitation of the cell, which is investigated in this work via analyzing characteristic discharge current plateaus and transition zones during the cells' over-discharge.<sup>3,4,12</sup> The tested cells revealed up to 24% cathode capacity overdimensioning estimated via DVA, whereas the NMC-811 cells showed a slightly increased overdimensioning (<+2%) compared to the NCA cells. During over-discharge, the cathode's capacity overdimensioning facilitates over-delithiation of the anode and copper dissolution until the over-saturation of the cathode is reached. This comes with a current and polarization drop<sup>4</sup> and leads to an overall attenuation of the physical processes.

The EIS characterization consists of a potentiostatic EIS protocol with nine points within 0% to 100% SoC at 25 °C within a climate chamber (KT 170, Binder, Germany). The chosen points were set at 3 V, 3.5 V, 3.6 V, 3.7 V, 3.8 V, 3.9 V, 4 V, 4.1 V, and 4.2 V for charge and discharge operation at 0.05C-CC and a CV period until 0.01C.

Next, the SLP cells are stored at 3.75 V under dry and low-temperature ( $T < 5$  °C) environment to slow down any degradation effects and enable a similar initial state for the short-circuit test. The preconditioning for the ESC and LSC tests includes initial cycles (see Table X) to exclude any influences of a non-finished formation and the storing process as applied in our previous work.<sup>12</sup>

Table III. ESC and LSC test protocols.

Capacity check-up			Chamber
Repetition	Sequence <sup>a)</sup>	Feature	Temperature
1×	CC <sub>CH</sub> -CV-R-CC <sub>DCH</sub> -R	Resting for 12 h CC: 0.1C, 3 V—4.2 V CV: <0.01C R: 15 min	25 °C
<b>Preconditioning</b>			
1×	CC <sub>CH</sub> -CV-R	CC: 0.2C, 3 V—4.2 V CV: <0.01C R: 2 h	25 °C
EIS at 4.2 V with 5 mV excitation voltage from 10 mHz to 200 kHz <sup>b)</sup>			
<b>Quasi-Isothermal short-circuit scenarios at 25 °C</b>			
Termination and measurement conditions of the calorimetric test bench (see Fig. 2)			
Resting for 12 h			
<b>Potentiostatic duration phase and measurement sampling frequency</b>			
	<b>ESC</b>		<b>LSC</b>
R	10 s at 1 Hz		10 s at 1 Hz
CV	5 s at 10 Hz	R	30 s at 10 kHz
ESC	10 s at 10 kHz	LSC	120 s at 100 Hz
	100 s at 100 Hz		20 h at 10 Hz
	$I_{sc} < 0.1$ mA at 10 Hz		
R	17 h at 1 Hz		
<b>Calorimetric duration phase and measurement sampling frequency</b>			
20 s at 1 kHz			
100 s at 100 Hz			
880 s at 10 Hz			
150 min at 1 Hz			
until end of potentiostatic measurement at 0.5 Hz			
EIS with 5 m V excitation voltage from 10 mHz to 200 kHz <sup>b)</sup>			

a) CC<sub>CH</sub> constant current charge CV constant voltage R rest/relaxation period CC<sub>DCH</sub> constant current discharge. b) 8 points per decade and 3 measurements per frequency.

Table IV. Potentiostatic results of the ESC tests applied to NCA and NMC-811 SLP cells.

Symbol Unit	$C_0$ <sup>c)</sup> mAh	$R_{Im(Z)=0.0}$ <sup>d)</sup> mΩ	$ Z _{1kHz,0}$ <sup>e)</sup> mΩ	$R_{ext}$ mΩ	$\frac{R_{ext}}{ Z _{1kHz,0}}$	$I_{max}$ mA	C-rate <sub>max</sub> —	$\Delta$ SoC %	$\frac{ Z _{1kHz,sc}}{ Z _{1kHz,0}}$ <sup>f)</sup>	$E_{sc,end}$ <sup>g)</sup> V
<b>Cell ID<sup>a)</sup></b>										
NCA#13	42.8	359	453	0 (° V)	0	8814	206	+38	2.2	0.6
NCA#18	43.5	311	395			8998	207	+35	2.4	2
NCA#24	41.5	357	479			7289	176	+56	3.1	0.7
NCA#21	42.3	348	430	50	0.12	5968	141	+42	2.1	1.7
NCA#22	43.5	349	449	50	0.11	7590	174	+73 <sup>h)</sup>	2	0.8
NCA#9	41.5	408	514	250	0.49	5913	142	+80 <sup>h)</sup>	1.8	0.6
NCA#11 <sup>b)</sup>	41.7	344	458	250	0.55	6371	153	+82 <sup>h)</sup>	1.8	0.5
NCA#7	40.8	367	450	500	1.11	4393	108	+46	1.2	1.1
NCA#20	41.8	411	496	500	1.01	3565	85	+50	1.5	1.1
NMC-811#3	38.6	328	408	0 (° V)	0	8456	219	+87 <sup>h)</sup>	2.2	0.4
NMC-811#4 <sup>b)</sup>	37.7	317	386			8938	237	+85 <sup>VI)</sup>	1.9	0.4
NMC-811#11	37.2	317	409			8699	234	+50	1.8	0.4
NMC-811#5	34.7	326	393	50	0.13	8030	231	+98 <sup>h)</sup>	2.5	3.2
NMC-811#24	38.9	322	387	50	0.13	7224	186	+51	1.6	0.7
NMC-811#7	38.9	318	436	250	0.57	6065	157	+83 <sup>h)</sup>	1.8	0.4
NMC-811#9 <sup>b)</sup>	38.7	296	409	250	0.61	6555	169	+86 <sup>VI)</sup>	1.3	0.4
NMC-811#10	37.4	303	387	500	1.3	4309	115	+85 <sup>h)</sup>	1.4	0.5
NMC-811#23	35.8	281	351	500	1.42	3709	104	+42	1.5	1.4

a) all SLP cells were visually inspected in the post-mortem analysis. b) used for SEM/EDX post-mortem analysis. c) from capacity check-up CC<sub>DCH</sub> (see Table III). d) impedance at 4.2 V and  $Im\{Z\}=0$  Ω. e) impedance at 4.2 V and 1 kHz. f) ref. to  $|Z|_{1kHz}$  before and after the short-circuit event. g) after a minimum of five days for relaxation. h) evaluated at 1E4 s due to a software issue of the potentiostat limiting the lower current limit.

The cyclic aging tests start right after the formation protocol. The cycling procedure included a  $1CC_{CH}-CV-R-CC_{DCH}-R$  sequence with a 15 min resting phase (R) and a charging CV phase until 1.5 mA ( $\approx 0.04C$ ) between 3.45 V and 4.1 V. This corresponds to an SoC range of  $\Delta 83.8\%$  starting from 6.7% and ending at 90.4% SoC for the NCA cells and an SoC range of  $\Delta 76.9\%$  between 5% and 81.9% SoC for the NMC-811 cells. The aging procedure was chosen to evoke a moderate aging rate and to avoid accelerated, non-linear aging behavior.<sup>28</sup> The restricted SoC range was chosen in reference to the major capacity gain vs the cell's terminal voltage within the full SoC range, which was derived from the analyzed OCV data. To determine the SoH points, a capacity check-up is designed incorporating a  $0.1CC_{CH}-CV-R-CC_{DCH}-R$  sequence with 10 min resting phase (R) and CV phases until 1.5 mA between 3 V and 4.2 V. The impedance was measured subsequently at 3.75 V, which follows the same procedure from Table X in the appendix. The capacity check-ups are applied every 25 cycles until a total of 75 cycles, every 50 cycles until a total cycle number of 175, and afterward until the end of the aging study every 100 cycles.

**ESC and LSC tests applied to SLP cells.**—The setup of the quasi-isothermal calorimetric test bench and the short-circuit test procedure are extensively described in our previous works<sup>3,12</sup> and are therefore not explained in further detail in this work. The applied calibration process, the calculation of the heat generation rate, and the dissipated heat are outlined in the supplementary part of this work. As result, the specific heat capacities of the NCA and the NMC-811 SLP cells were estimated to  $800.5 \text{ J kg}^{-1}\text{K}^{-1}$  and  $866.6 \text{ J kg}^{-1}\text{K}^{-1}$ , which is well in line with comparable pouch-type cells.<sup>3</sup>

Moreover, the different short-circuit events are explained in the following. Figure 2 shows the calorimetric test bench together with the three different potentiostatic measurement procedures of this work. The first procedure describes the potentiostatic setup of ESC tests without (i.e.  $0 \text{ V} \approx 0 \text{ m}\Omega$ ) or with (i.e.  $50 \text{ m}\Omega$ ,  $250 \text{ m}\Omega$ , or  $500 \text{ m}\Omega$ ) an external resistance (see ESC in Fig. 2). Here, the source measurement unit (SMU, B2901A, Keysight Technologies, USA) is used to measure the cell's terminal voltage  $E_{sc}$  between the cathode and anode, whilst the potentiostat (SP-300 with 10 A booster, BioLogic Science Instruments, France) applies a 0 V condition during the ESC test and measures the discharge current flow  $I_{sc}$ .

The second procedure describes the potentiostatic setup of LSC tests, where the SMU measures the electrical potential  $\Phi_{sc}$  between the electrically-contacted stainless-steel needle (2R2 of  $\varnothing 1 \text{ mm}$ , Unimed, France) and the cell's negative tab. The potentiostat measures the terminal voltage  $E_{sc}$  (see LSC in Fig. 2). The LSC test is initiated via a manual trigger for the needle penetration.

The third procedure describes the ESC test for SLP cells with lithium reference electrode setup, where a second potentiostat (SP-300, BioLogic Science Instruments, France) measures the electrical potential between the cell's negative tab versus the lithium reference tab (see Figs. 1 and 2). Besides, the setup is identical to the ESC procedure with standard SLP cells. For all tests, the temperature of the copper bars ( $T_{cu,i}$ ,  $i = \text{top, bottom}$ ) and the SLP cell  $T_c$  are measured with three digital multimeters (DMM, 34 470A, Keysight Technologies, USA) to calculate the heat generation rate and the overall dissipated heat. The used Pt100 sensors have an accuracy of  $\pm 0.15 \text{ K}$  at  $0^\circ\text{C}$  (DIN/IEC Class A).<sup>2</sup> The test bench is incorporated in a climate chamber, where the  $25^\circ\text{C}$  temperature is controlled via resistive heating and Peltier-cooling at a temperature accuracy of  $\pm 0.03 \text{ K}$ .<sup>2</sup>

Table III summarizes the ESC and LSC test protocols. After 12 h of thermal preconditioning, a capacity check-up determines the initial capacity  $C_0$  of the SLP cells, as the discharge current  $I_{sc}$  during the short-circuit event is normalized to the initial capacity  $C_0$  (see Fig. 3). Next, the preconditioning sets all SLP cells of this work to an SoC level of 100% (i.e. 4.2 V). The EIS applied at 4.2 V is used to derive the initial impedances ( $R_{\text{Im}(Z)=0,0}$ ,  $|Z|_{1\text{kHz},0}$ ). After sufficient thermal relaxation of at least 12 h of the test setup, the ESC

or LSC test procedures start with the respective sampling rates for the potentiostatic and calorimetric test equipment, as summarized in Table III. All short-circuit tests are conducted at a fully charged state (i.e. 100%) and at  $25^\circ\text{C}$ . At the end of the short-circuit test, a final EIS is applied to determine the impedance increase due to the short-circuit event.

**Post-mortem analysis.**—The post-mortem part of this work investigates selected NCA and NMC-811 SLP cells in order to qualitatively investigate effects of cell, electrode, and active material degradation and especially study the effect of copper dissolution and deposition, which occurs during the applied short-circuit tests.<sup>3,4,12</sup> Visual inspection, photographic and/or digital-microscopic (Omni Core, Ash Technologies, Ireland) images are taken from all cells, which were opened and dismantled after the short-circuit tests. Selected SLP cells are opened and dismantled in an argon-filled glove box ( $\text{H}_2\text{O}$ ,  $\text{O}_2 < 0.1 \text{ ppm}$ , MBraun, Germany) to extract samples for scanning electron microscopy (SEM) and energy-dispersive X-ray spectroscopy (EDX) measurements. The samples are washed with diethyl carbonate (DEC) and dried before applying SEM and EDX analysis (JCM-600 or JSM-IT200 InTouchScope, JEOL, Germany) at 15 kV acceleration voltage.

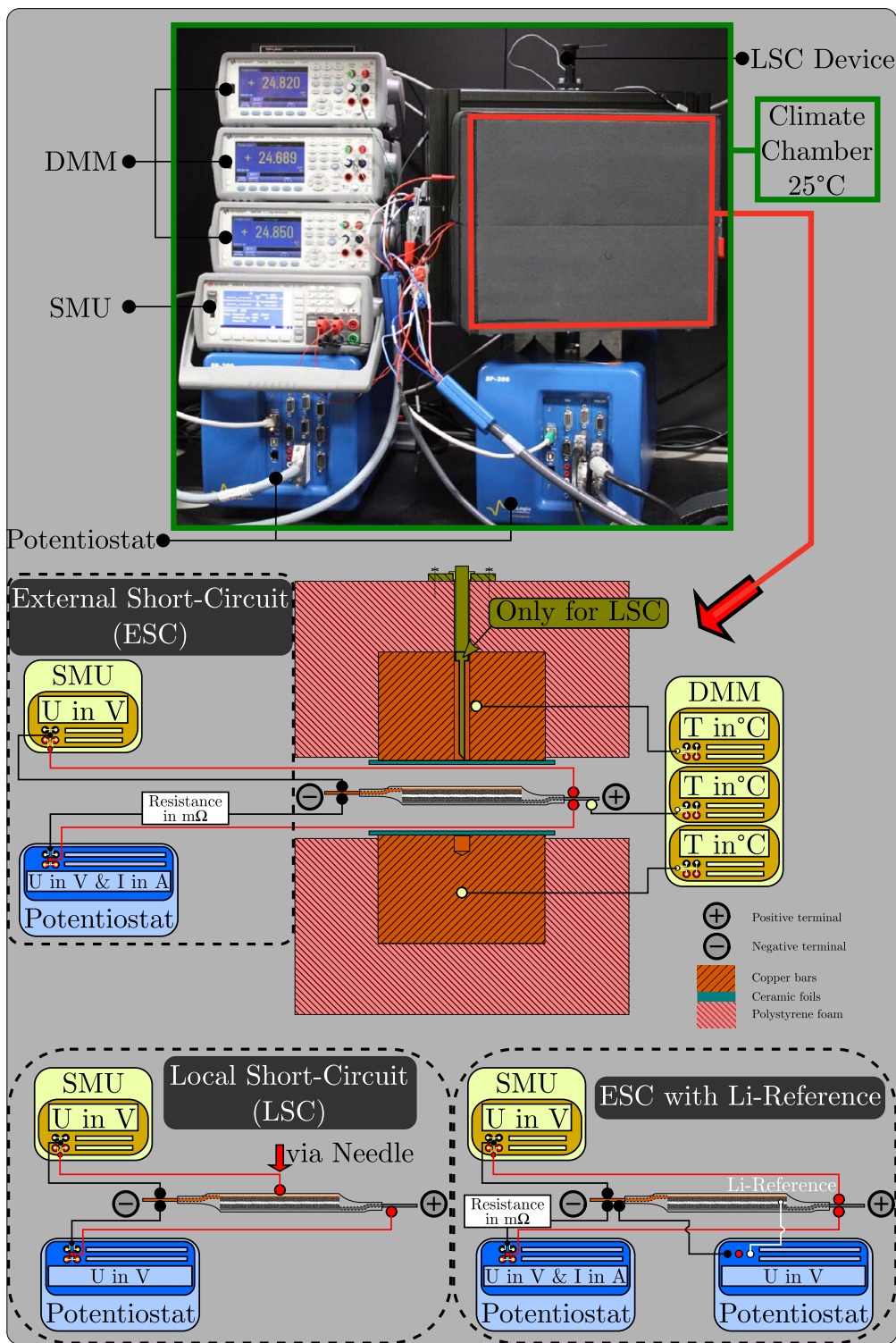
## Results and Discussion

In this section the potentiostatic and calorimetric ESC test results with different external resistances, the LSC tests results triggered by a needle, the ESC tests results with aged cells, and ESC tests results with lithium metal reference electrodes are presented. Conclusively, the post-mortem analysis results are discussed.

**ESC applied to NCA and NMC-811 SLP cells.**—The cells presented in this section contained no reference electrodes and underwent no cyclic aging procedure. In total, 18 ESC tests were applied to the silicon-graphite/nickel-rich SLP cells to study the dependency of the short-circuit intensity on the external resistance  $R_{\text{ext}}$ <sup>3,12</sup> and to analyze the electrochemically-caused rate-limiting effects<sup>3,6</sup> causing characteristic plateaus and transition zones of current, cell voltage, and heat generation rate. Several 0 V-,  $50 \text{ m}\Omega$ -,  $250 \text{ m}\Omega$ -, and  $500 \text{ m}\Omega$ -tests were conducted within this ESC study with the NCA and NMC-811 SLP cells and the key results are summarized in Table IV. The mean initial capacity  $C_0$  lies within the range of  $42.2 \pm 0.9 \text{ mAh}$  and  $37.5 \pm 1.4 \text{ mAh}$  (i.e.  $\pm$  standard deviation) for the NCA and NMC-811 cells. The initial impedance at 1 kHz  $|Z|_{1\text{kHz},0}$  reveals mean values of  $458 \pm 35 \text{ m}\Omega$  and  $396 \pm 23 \text{ m}\Omega$ , which suggests a slightly lower impedance of the NMC-811 cells compared to the NCA cells. The initial cell capacity and initial impedance of each individual cell are summarized in Table IV. The slightly lower capacity of the NMC-811 cells suggests a different formation behavior with the used electrolyte compared to the NCA cells, which should be investigated further in future studies but its discussion is out of scope for this work. The appearing variance in capacity and resistance is most likely caused by the manual manufacturing process of the SLP cells.

As observed in previous studies, the ESC intensity is dominated by the initial capacity and the impedance of the cell.<sup>3,12</sup> Lower values for both trigger higher C-rates, accelerate the shorting scenario and thus increase the short-circuit intensity. Furthermore, the intensity can also be controlled by the external resistance especially in the very beginning of the shorting (i.e.  $< 1 \text{ s}$  after short-circuit initiation),<sup>3,12</sup> where the  $50 \text{ m}\Omega$ -,  $250 \text{ m}\Omega$ -, and  $500 \text{ m}\Omega$ -case superimpose approximately 12%, 50% to 60%, and up to 111% to 142% more as the actual 1 kHz impedance of the cells (see  $\frac{R_{\text{ext}}}{|Z|_{1\text{kHz},0}}$  in

Table IV). In the case of the 0 V condition, only the impedance of the cell affects the initial intensity. Considering the active electrode area of the tested SLP cells ( $A_{\text{act}} = 16.35 \text{ cm}^2$ ), the external resistances can be weighted to  $0.0818 \text{ m}\Omega \text{ m}^2$  ( $50 \text{ m}\Omega$ ),  $0.4088 \text{ m}\Omega \text{ m}^2$  ( $250 \text{ m}\Omega$ ), and  $0.8175 \text{ m}\Omega \text{ m}^2$  ( $500 \text{ m}\Omega$ ). For



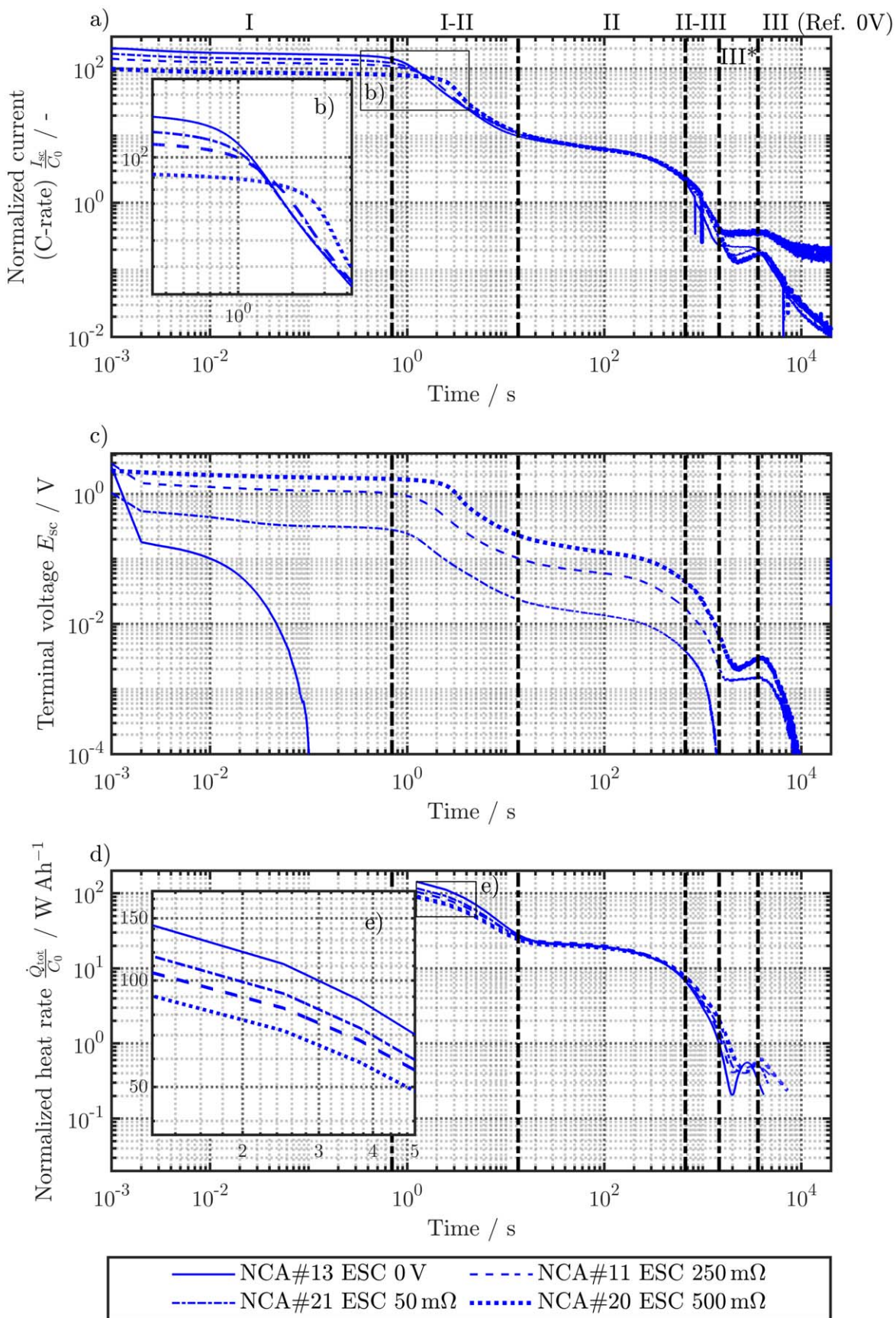
**Figure 2.** Schematic view of the calorimetric test bench for ESC (middle and right) and LSC (left) tests applied to the pouch-type cells depicted in the center of each configuration. The test bench is placed inside a climate chamber at 25 °C and the potentiostatic (potentiostat, SMU) and calorimetric (DMM) measurement devices are depicted with their respective sensor locations. For the LSC tests, the penetration procedure using the short-circuit device with the penetration needle is shown in the lower left part.

example, a fictive, scaled-up NCA pouch cell with 0.8 m<sup>2</sup> of active electrode area would result in around 20 A h of capacity and the applied ESC conditions would correspond to an external resistance of 0.1 mΩ, 0.5 mΩ, and 1 mΩ.

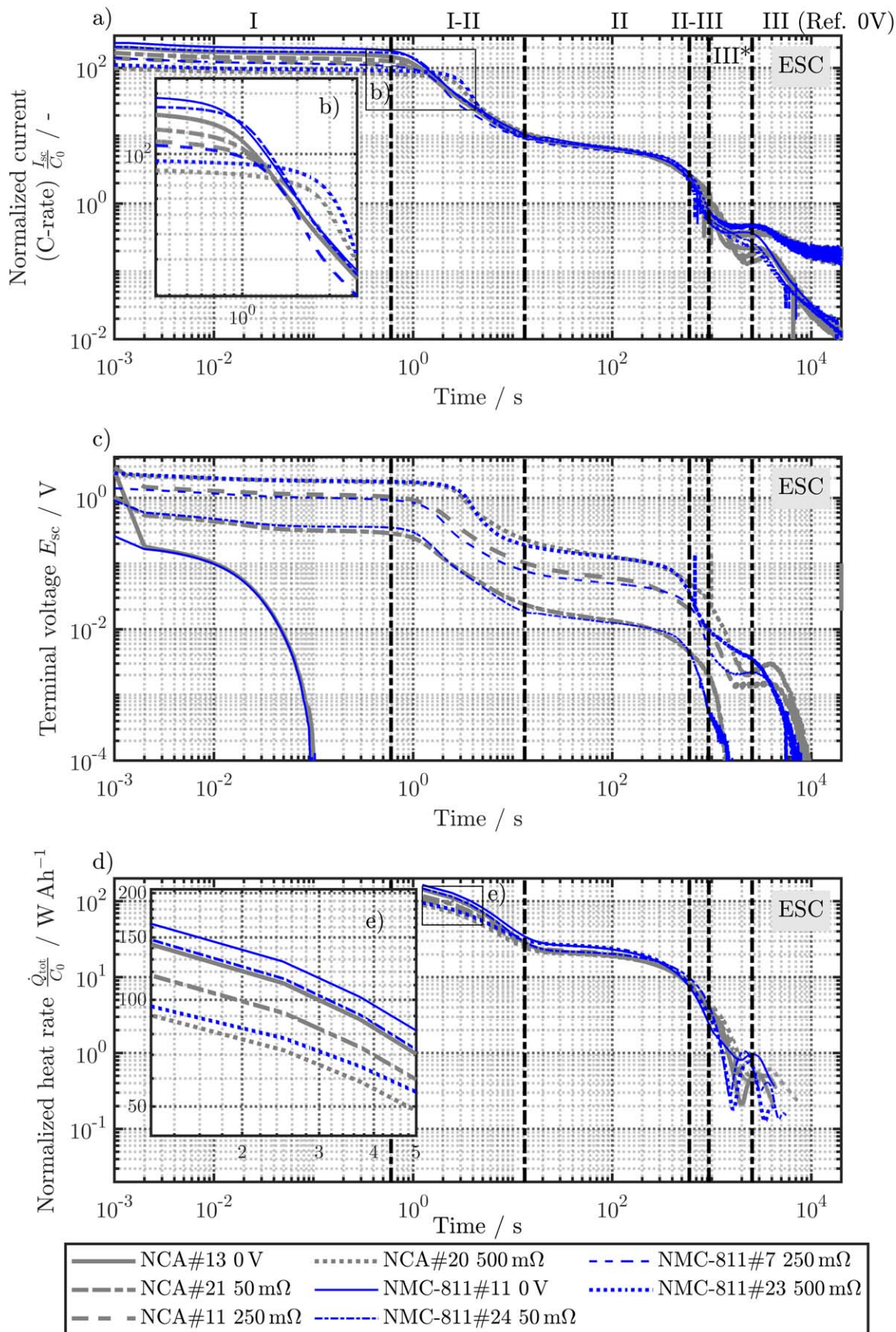
As a result of the lower capacity and impedances of the NMC-811 cells, accelerated short-circuits appear, and regarding all ESC tests in Table IV, increased C-rates appear compared to the NCA

cells. Up to 237C (8.938 A) appear for cell NMC-811#4 compared to the maximum of 207C (8.998 A) for NCA#18 for the 0 V-case. For increasing external resistances, the maximum currents and thus the short-circuit intensity decreases for both NMC-811 and NCA cells, as can be seen in Table IV. The over-discharge<sup>3,12</sup> calculated in Δ SoC of the initial capacity for all cells ranges from 38% to 56%, where unfortunately due to a software issue some experiments



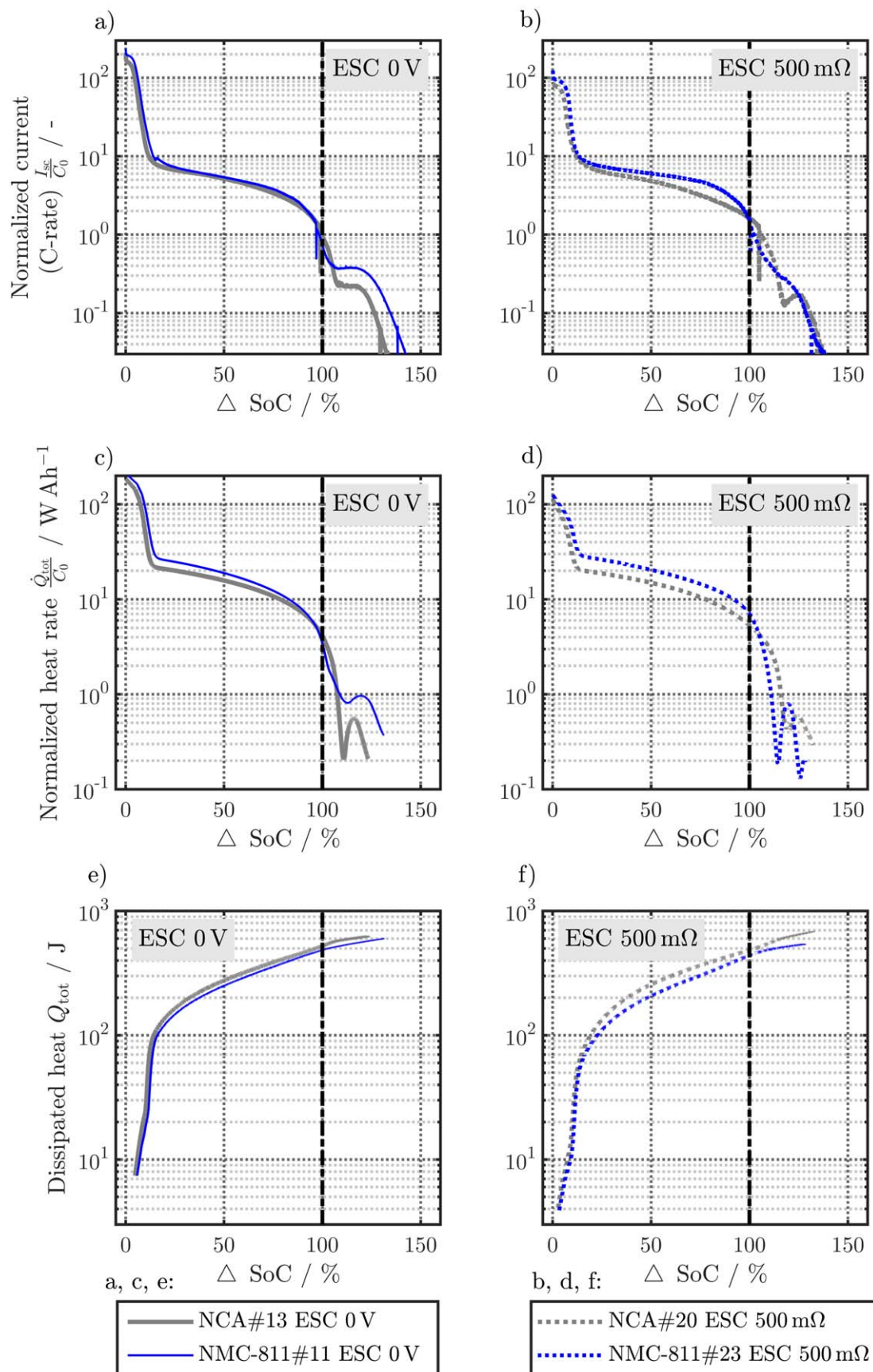


**Figure 3.** Test results over time of normalized current  $\frac{I_{sc}}{C_0}$  (a,b), terminal voltage  $E_{sc}$  (c), and normalized heat generation rate  $\frac{\dot{Q}_{tot}}{C_0}$  (d,e) during four different ESC conditions of 0 V (NCA#13), 50 mΩ (NCA#21), 250 mΩ (NCA#11), and 500 mΩ (NCA#20). The tested SLP cells were of SiC/NCA type. The plateaus and transition zones (I, I-II, II, II-III, III\*, and III) are determined for the current profile of the 0 V case (NCA#13) and depicted in the plots a), c), and d). The magnifications b) and e) show the difference in current and heat generation profile depending on the applied ESC condition.



**Figure 4.** Test results over time of normalized current  $\frac{I_{sc}}{C_0}$  (a,b), terminal voltage  $E_{sc}$  (c), and normalized heat generation rate  $\frac{\dot{Q}_{tot}}{C_0}$  (d,e) during four different ESC conditions of 0 V (NMC-811#11), 50 mΩ (NMC-811#24), 250 mΩ (NMC-811#7), and 500 mΩ (NMC-811#23). The depicted SiC/NMC-811 cells (blue lines) are compared to the SiC/NCA cells (gray lines) of Fig. 3. The plateaus and transition zones (I, I-II, II, II-III, III\*, and III) are determined for the current profile of the 0 V case (NMC-811#11) and depicted in the plots a), c), and d). The magnifications b) and e) show the difference in current and heat generation profile depending on the applied ESC condition.





**Figure 5.** Test results over the withdrawn  $\Delta \text{SoC}$  of normalized current  $\frac{I_{sc}}{C_0}$  (a,b), normalized heat generation rate  $\frac{\dot{Q}_{tot}}{C_0}$  (c,d), and total dissipated heat  $Q_{tot}$  (e,f) during two different ESC conditions of 0 V (NCA#13 and NMC-811#11) on the left and 500 mΩ (NCA#20 and NMC-811#23) on the right side. The SiC/NMC-811 cells (blue lines) are compared to the cells SiC/NCA cells (gray lines). Exceeding the initial capacity  $C_0$  is marked at 100%  $\Delta \text{SoC}$  (black dash-dot line) and marks the onset of over-discharge.

**Table VI. Potentiostatic results of the LSC tests with a 1 mm needle using standard SLP cells.**

Symbol Unit	$C_0^c)$ mAh	$R_{\text{Im}(\underline{Z})=0,0}^d)$ m $\Omega$	$ \underline{Z} _{1\text{kHz},0}^e)$ m $\Omega$	$\varnothing$ $d_{\text{Needle}}$ mm	$\frac{ \underline{Z} _{1\text{kHz},\text{sc}}^f)}{ \underline{Z} _{1\text{kHz},0}}$	$E_{\text{sc,end}}^g)$ V
<b>Cell ID<sup>a)</sup></b>						
NCA#2 <sup>b)</sup>	37.7	359	482	LSC: 1	1.5	0.3
NCA#8 <sup>b)</sup>	42.9	446	541		2.7	0.4
NCA#10	42.3	315	446		4.8	0.3
NMC-811#2	35.4	267	336	LSC: 1	2.3	0.1
NMC-811#6	31.3	402	535		4.8	0.2
NMC-811#8 <sup>b)</sup>	39.1	282	337		1.3	0.2

a) All SLP cells were visually inspected in the post-mortem analysis. b) used for SEM/EDX post-mortem analysis. c) from capacity check-up  $CC_{\text{DCH}}$  (see Table III). d) Impedance at 4.2 V and  $\text{Im}\{\underline{Z}\} = 0$ . e) Impedance at 4.2 V and 1 kHz. f) ref. to  $|\underline{Z}|_{1\text{kHz}}$  before and after the short-circuit event. g) after a minimum of five days for relaxation.

were biased leading to exceeding levels in over-discharge, which are neglected here. The final impedance rise after termination of the short-circuit lies in the range of 1.2 (NCA#7 ESC 500 m $\Omega$ ) to 3.1 (NCA#24 ESC 0 V) for all evaluated tests, which suggest a decreasing trend from high (0 V) to low (500 m $\Omega$ ) intensity. Most likely, the higher C-rates and thus the increased intensity of the short-circuit leads to a higher level of degradation within the cell resulting in the observed trend. The relaxed terminal voltages after the short-circuit vary in a range from 0.4 V to 3.2 V for all tested cells. In general, the short-circuit intensity of the NMC-811 cells tends to higher initial current plateaus and indicates therefore a higher short-circuit intensity, which is caused by the lower impedances and capacities<sup>3</sup> resulting after the formation procedure compared to the NCA cells.

Focusing on the variance of intensity during the ESC applied to NCA cells, exemplary cells NCA#13 (0 V), NCA#11 (50 m $\Omega$ ), NCA#21 (250 m $\Omega$ ), and NCA#20 (500 m $\Omega$ ) are discussed in Fig. 3 in terms of the normalized short-circuit current (see Fig. 3a+3b), the decrease of the terminal voltage (see Fig. 3c), and the heat generation rate (see Fig. 3d+3e). Hereby all characteristic plateaus and transition zones of current, voltage, and heat generation during the short-circuit are evaluated according to our previous works.<sup>4,12</sup> For the readers' convenience, we briefly describe the previous categorization<sup>4,12</sup> and add the findings of this work in the following:

- **Plateau I:** Ohmic losses mainly in the liquid electrolyte dominate the polarization behavior in the entire electrode stack (i.e. anode, separator, and cathode domain) and very likely limiting of anode deintercalation kinetics occurs.

- **Transition I-II:** Increase of polarization caused by electrolyte depletion in the pore of the cathode domain and possibly active particle depletion in the anode domain lead to a decrease of the current and the terminal voltage.

- **Plateau II:** Mass transport limitations in the solid cathode domain possibly at the active particle surface (i.e. saturation due to solid-phase diffusion limitation) near the separator interface and in the liquid pore (i.e. depletion of the electrolyte) near the current collector, which leads to saturation of the cathode particles (i.e. NMC-111) at the end.

- **Transition II-III:** Depletion of the active particles' surfaces in the anode domain causing an additional drop of the current and the terminal voltage, which is accompanied by copper dissolution from the anode's current collector caused by the increasing potentials in the anode domain.

- **Plateau III\*:** Additional current plateau observed for the SiC/NCA and SiC/NMC-811 cells compared to the G/NMC-111 SLP cells, most likely caused by a delayed saturation of the nickel-rich cathode particles as the balancing revealed in both cases an oversized cathode in terms of capacity.

- **Plateau III:** Ongoing de- and intercalation reactions accompanied by copper dissolution and final attenuation of all physical processes.

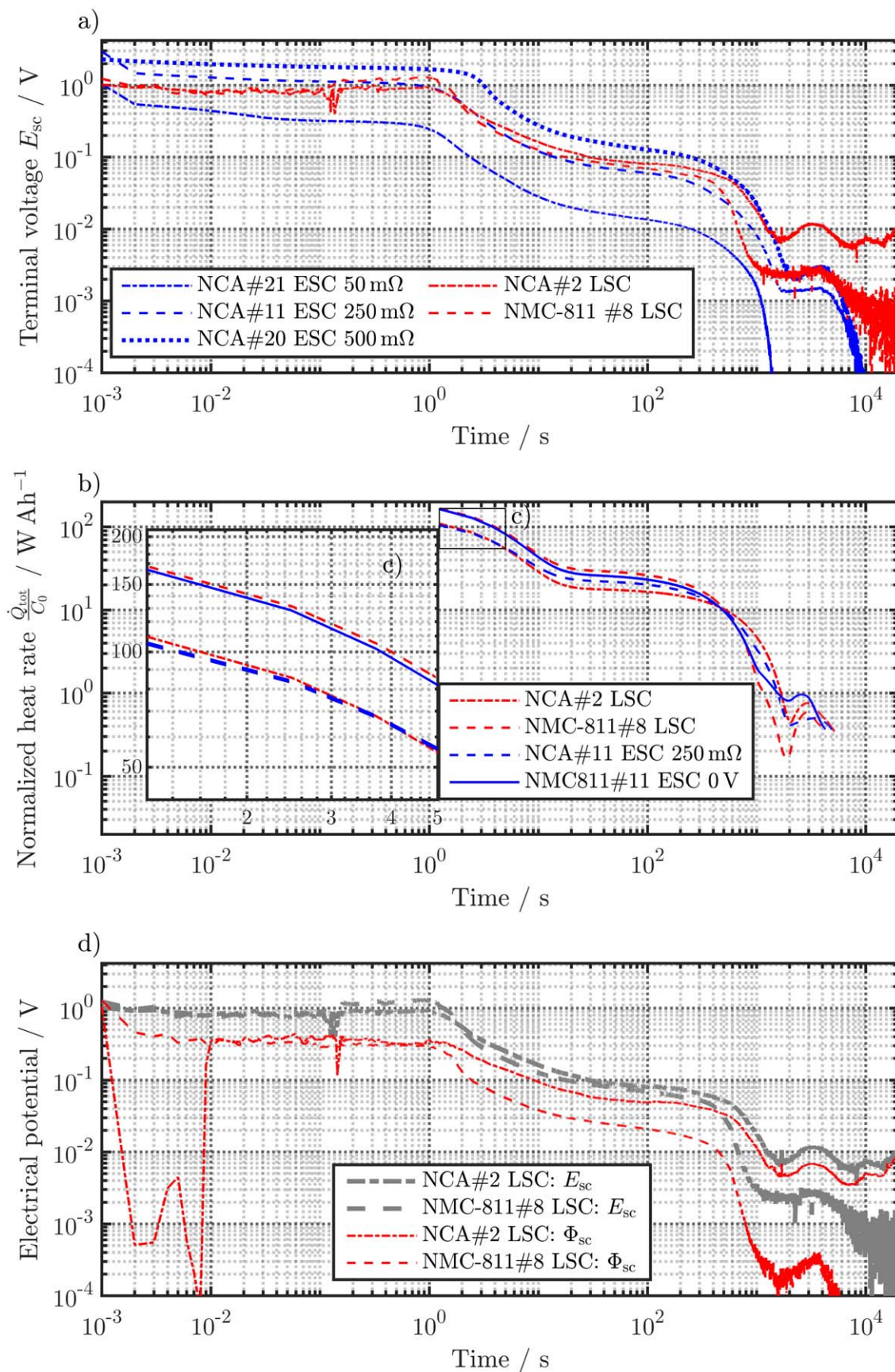
The categorization can be applied to all NCA test cells of this work as well as shown in Fig. 3 following the profile of the short-circuit current for the 0 V case (NCA#13). Even if the categorization was analyzed for a G/NMC-111 chemistry,<sup>4</sup> a quite similar behavior for the SiC/NCA chemistry can be observed showing nearly identical plateaus and transition zones. As the cell design of the G/NMC-111, SiC/NCA, and SiC/NMC-811 SLP cells were designed in a similar way (see Table II) and the chosen chemistries are comparable (i.e. graphite-type anode and transition metal oxide cathodes), a quite similar behavior during the short-circuit can be expected and is observed within this work.

However, a distinct difference appears right before the onset of plateau III, as seen in Fig. 3a). A new plateau III\* appears for the silicon-containing, nickel-rich NCA cells, which is missing for the G/NMC-111 case. This additional plateau was similarly seen for the tested SiC/NMC-811 cells (see Fig. 4). Analyzing the balancing of both NCA and NMC-811 cells via applying DVA, a capacitively oversized cathode appears compared to the anode in both cases (see balancing from DVA in the supplementary material of this work). The effect of an over-dimensioned cathode compared to the G/NMC-111 with an over-dimensioned anode<sup>3</sup> is the extension of saturation of the cathode particles appearing in the third plateau III\* after the transition II-III, where the anode particle surfaces have already depleted and the current and electrical potentials have decreased. In consequence, the ongoing discharge leads to an early

**Table V. Plateaus and transition zones during the ESC tests for NCA and NMC-811 cells with respect to the withdrawn  $\Delta$  SoC.**

Stage	I	I-II	II	II-III	III*	III
<b>Cell ID</b>	<b>ESC</b>					
<b>NCA</b>	$\Delta$ SoC/%					
NCA#13	0 V	3	11.9	$\approx 92.1$	107.1	118.8
NCA#20	500 m $\Omega$	4.4	11.7	$\approx 90.1$	116.3	126.7
<b>NMC-811</b>						
NMC-811#11	0 V	3.2	13.7	$\approx 91.2$	101.7	119
NMC-811#23	500 m $\Omega$	4.5	13.2	$\approx 96.9$	107	123.4





**Figure 6.** Test results over time of terminal voltage  $E_{sc}$  (a), normalized heat generation rate  $\frac{\dot{Q}_{tot}}{C_0}$  (b,c), and measured electrical potentials ( $E_{sc}$  and  $\Phi_{sc}$ , d) during LSC condition of the NCA#2 and NMC-811#8 cell in reference to chosen NCA (#21, #11, and #20) and NMC-811 (#11) ESC test results of different short-circuit intensity. The electrical potential  $\Phi_{sc}$  was measured between the cell's negative tab and the electrically contacted needle.

**Table VII. Results of the cyclic aging study for SLP cells with and without reference electrodes.**

Symbol	$C_0^{a)}$ mAh	EfC <sup>b)</sup> —	SoH <sup>c)</sup> %	$\Delta  Z _{1\text{kHz}}^{d)}$ %
<b>Cell ID</b>				
NCA#17 <sup>ref</sup>	42	1045	74.8	+22
NCA#19	43	974	75.3	+17
NMC-811#20	35.7	1454	76.9	+12
NMC-811#22 <sup>ref</sup>	36.5	793	78.1	+11

a) from 2<sup>nd</sup> CC<sub>DCH</sub> during the initial cycles (see Table X). b) Equivalent full cycles (i.e. ref. to  $C_0$ ) of 1C-CC<sub>DCH</sub>-R-0.5C-CC<sub>CH</sub>-CV-R cycling with 15 min resting phase (R) and a charging CV-phase until 1.5 mA ( $\approx 0.04C$ ) between 3.45 V and 4.1 V. c) ref. to  $C_0$ . d) Increase of impedance at 3.75 V and 1 kHz before and after the cyclic aging study.

onset of possible copper dissolution as the anode potentials increase with ongoing delithiation. As a consequence, the NCA and NMC-811 cells in this work are expected to trigger more copper dissolution than the NMC-111 cells.

Regarding Fig. 3a, the initial current levels in plateau I represent the intensity of the shorting, as 206C, 181C, 153C, and 107C appear for the 0 V, 50 m $\Omega$ , 250 m $\Omega$ , and 500 m $\Omega$  case. The plateaus and transition zones are indicated for the 0 V case according to the rules presented in our previous work.<sup>2</sup> Plateau I decreases to 140C and 70C until 0.7 s and 2.05 s for the 0 V and the 500 m $\Omega$  case, where the transition zone I-II initiates. Consequently, the high-current phase lasts approximately three times longer for the 500 m $\Omega$  case. The magnification in Fig. 3b highlights the transition from plateau I to transition zone I-II and shows the delayed transition for lower short-circuit intensities correlating well with the higher external resistances. Hereby, the 50 m $\Omega$  and 250 m $\Omega$  cases range in between the 0 V and the 500 m $\Omega$  cases, which is why only the 0 V and the 500 m $\Omega$  case are discussed further. The transition zone I-II ends at 13.4 s and 15 s, and the second current plateau II reaches 9.8C and 10.5C at the beginning and decreases to 2.1C and 1.9C at approximately 660 s for the 0 V and the 500 m $\Omega$  case. Again, the 500 m $\Omega$  case reveals a longer exposure time at the second current plateau II. Overall, all ESC cases are approximately at the same current level during plateau II, independently of the ESC condition, the initial impedance, and the capacity of the cells. The transition II-III ends at 1460 s (0 V) and 2180 s (500 m $\Omega$ ) with current levels of 0.2C and 0.1C.

The plateau III\* lasts until 3630 s (0 V) at a rather constant current level and the 500 m $\Omega$  case reveals a similar current plateau starting at  $\approx 2000$  s and ending at 4080 s. In case of the 250 m $\Omega$ , unfortunately, a software issue of the potentiostat limited the lower current resolution, which is why the depicted current profile in Fig. 3a shows a higher level than the remaining cases. After plateau III\*, attenuation of the physical processes initiates until the end of the test, which is limited to 100  $\mu\text{A}$  or in case of the potentiostat's software issue, the tests were evaluated until 10<sup>4</sup> s. In case of the software issue, the current range was not automatically adjusted, leading to an earlier termination of the measurement.

A novel current plateau III\* at low current rate levels around 0.1C to 0.2C appears compared to previously investigated NMC-111 cells,<sup>4,12</sup> which is most likely caused by the different cell balancing with an overdimensioned cathode for NCA and NMC-811 instead of overdimensioned anode for NMC-111. In general, the higher the external resistance, the lower the short-circuit intensity appears with a lower initial current plateau I and the longer the current plateau I can be sustained until the transition zone I-II. After passing transition zone I-II, the short-circuit cases behave rather similarly with respect to normalized current levels independent from the applied external short-circuit condition until the end of the test.

Figure 3c shows the terminal voltage profiles during the four ESC cases. All voltage profiles start from 4.2 V and proceed during the

ESCs according to the current profile in Fig. 3a and the aforementioned plateaus and transition zones. The variance in short-circuit intensity depending on the applied ESC condition appears as expected. The higher the intensity, the earlier the terminal voltage decreases, where only the high ohmic ESCs (i.e. 250 m $\Omega$ , and 500 m $\Omega$ ) show clearly each of the aforementioned plateaus and transitions zones. The low ohmic ESC approach reaches the low voltage limits earlier (i.e.  $<100 \mu\text{V}$ ) which falls in the range of the measurement accuracy of the potentiostats. Following this, a clear difference between the voltage profiles of the ESC cases appears during plateau II, whereby the discharge current ranges around the same magnitude.

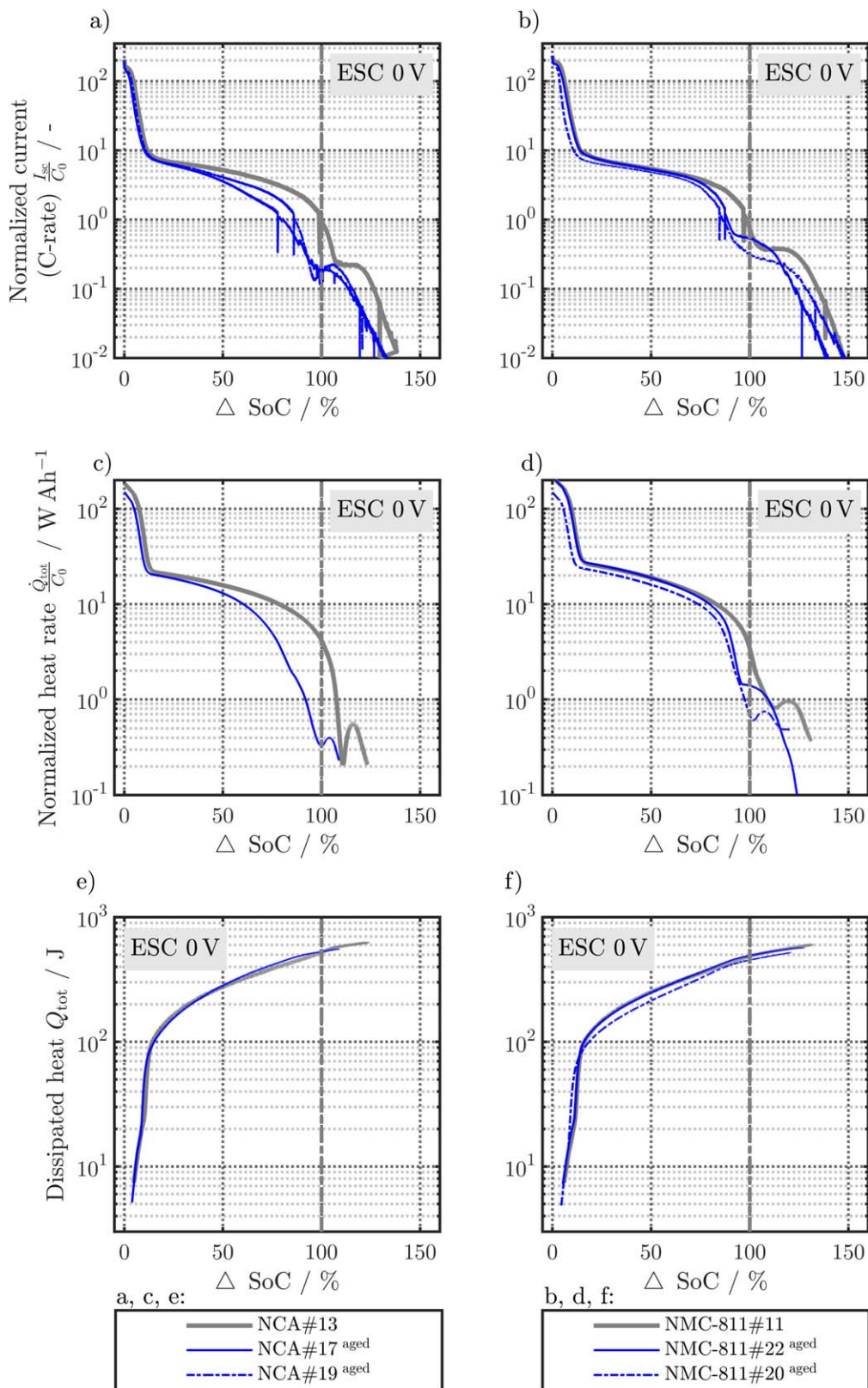
Figure 3d shows the normalized heat generation rate, which follows the current profile with a certain time delay due to the thermal inertia of the test setup.<sup>4,12</sup> The magnification in Fig. 3e shows similar to Fig. 3b the difference of short-circuit intensity. The lower external resistance and consequently the higher the short-circuit intensity becomes the higher the observed heat generation rate gets. At the very beginning, 143 W Ah<sup>-1</sup>, 117 W Ah<sup>-1</sup>, 105 W Ah<sup>-1</sup>, and 90 W Ah<sup>-1</sup> appear for the four cases. During plateau II, levels around 21 W Ah<sup>-1</sup> are reached, and close to the end during plateau III\* approximately 0.6 W Ah<sup>-1</sup> appear at maximum for all ESC cases. During plateau III\*, the trend of the terminal voltage is similar to the current profile.

Referring to the aforementioned, fictive 20 A h NCA cell with an active material area of 0.8 m<sup>2</sup>, these results of the heat generation rate would correspond to approximately 2.9 kW for the 0 V case at the very beginning, 0.4 kW during plateau II, and 0.012 kW at a maximum during plateau III\*. The total dissipated heat of the investigated SLP cells sums up to 625 J for the 0 V case and the remaining ESC cases appear in a similar magnitude as the capacities of the SLP cells are quite similar. The total amount of dissipated heat tends to increase with increasing capacity of the cells, which confirms a dominant but rather straightforward influence of the capacity on the generated heat, as found in our previous work.<sup>4</sup> Note, that the heat generation rate and the total dissipated heat refer to the quasi-isothermal test condition excluding any additional exothermal side reactions.<sup>4</sup> The profile of the heat generation rate follows the current flow profile and the total dissipated heat is similar with a marginal variance caused by the cell's capacity, which reveals a dominant influence on the total amount of dissipated heat.

Similar to the studied NCA cells, four ESC tests at the aforementioned ESC conditions are selected from the NMC-811 tests and shown in Fig. 4 in comparison to the results gained from the NCA cells, as shown in Fig. 3. The lower capacities and impedances (see Table IV) lead to higher, initial C-rates compared to the NCA cells, as shown in Fig. 4a and in the magnification Fig. 4b. Besides, very similar plateaus and transition zones as seen for the NCA tests appear, which can also be clearly seen in the profile of the terminal voltage (see Fig. 4c) and the heat generation rate (see Figs. 4d and 4e).

Interestingly, the plateau III\* shows C-rates of around 0.4C, which lies higher than for the NCA cells. In addition, most ESC tests (i.e. 0 V, 50 m $\Omega$  and 500 m $\Omega$ ) show a less distinct III\* plateau than the NCA cells, and unfortunately, the 250 m $\Omega$  test was biased by the aforementioned software issue of the potentiostat as well. As the difference between the NCA and the NMC-811 cells is only the embedded cathode, the alteration of the III\* plateau can most likely be ascribed to cathode-related polarization. Moreover, the solid diffusion in the cathode particles may also be different for the NCA and NMC-811 technologies. Considering the lower capacities of the NMC-811 cells, a slightly shorter duration of the current plateau III\* and the remaining plateaus appear, which is well in line with the findings of our previous work.<sup>4</sup> Regarding the heat generation rate in Fig. 4d and the magnification Fig. 4e, similar plateaus as for the NCA cells appear and higher initial heat generation rates (i.e. +15% for 0 V and +7% for 500 m $\Omega$ ) appear due to the increased initial current flow. The total amount of heat for the 0 V case (NMC-811#11, 37.2 m Ah and NMC-811#23, 35.8 m Ah) accounts for



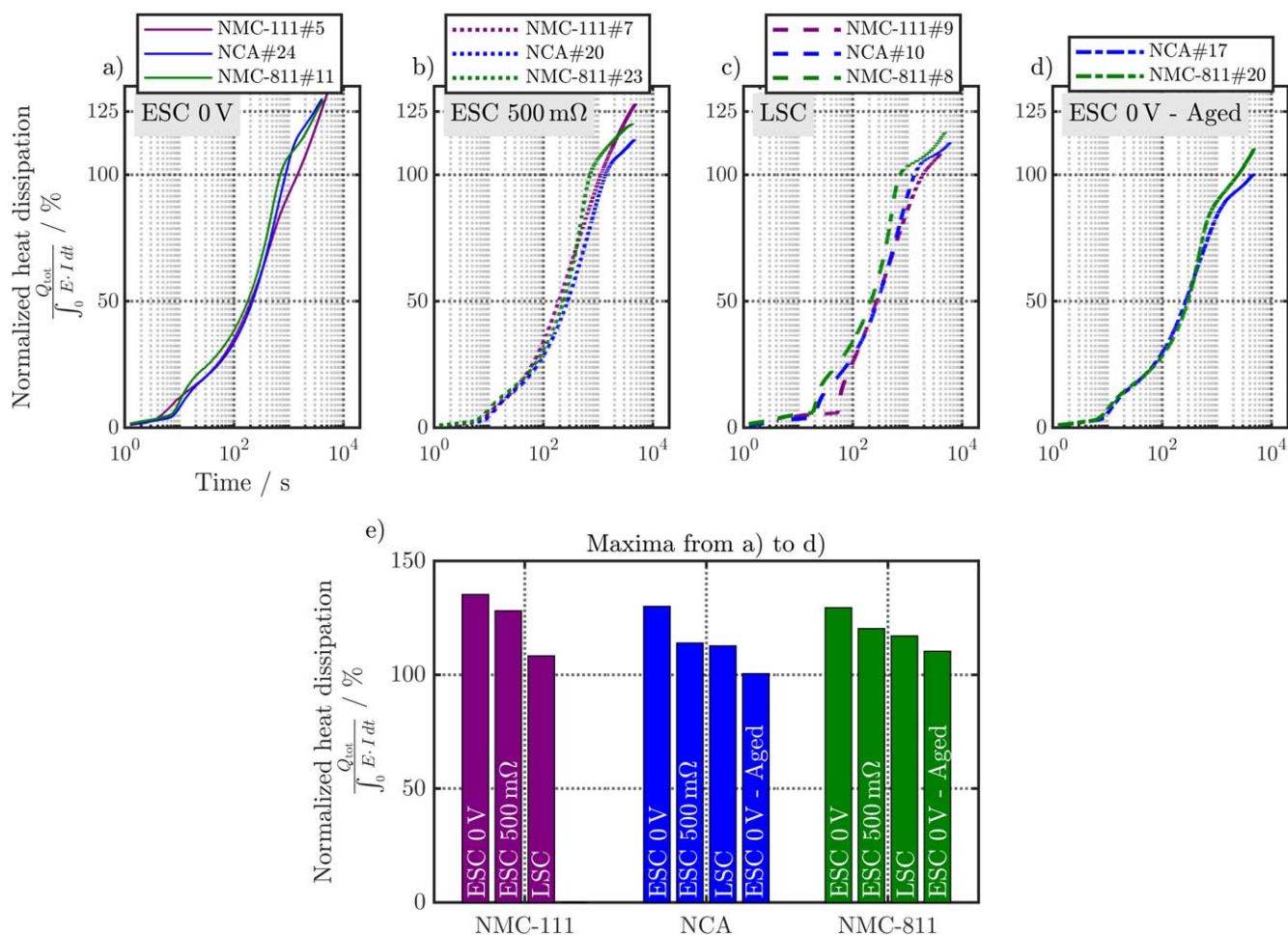


**Figure 7.** Test results over withdrawn  $\Delta \text{SoC}$  of normalized current (C-rate)  $\frac{I_{sc}}{C_0}$  (a,b), normalized heat generation rate  $\frac{\dot{Q}_{tot}}{C_0}$  (c,d), and dissipated heat  $Q_{tot}$  (e,f) during ESC 0 V condition of aged NCA (#17 with reference electrode,#19) and NMC-811 (#20,#22 with reference electrode) cells in reference to the non-aged NCA#13 and NMC-811#11 cells. Due to malfunction of the measurement equipment no heat generation rate and dissipated heat could be measured for SLP cell NCA#19.

**Table VIII. Potentiostatic results of the 0 V ESC tests applied to aged SLP cells with and without reference electrode.**

Symbol Unit	$C_0$ <sup>c)</sup> mAh	$R_{ImZ=0.0}$ <sup>d)</sup> m $\Omega$	$ Z _{1kHz,0}$ <sup>e)</sup> m $\Omega$	$I_{max}$ mA	C-rate <sub>max</sub> —	$\Delta$ SoC %	$\frac{ Z _{1kHz,sc}}{ Z _{1kHz,0}}$ <sup>f)</sup>	$E_{sc,end}$ <sup>g)</sup> V
<b>Cell ID<sup>a)</sup></b>								
NCA#17 <sup>ref,b)</sup>	42	323	449	6631	158	+27	2.5	0.7
NCA#19 <sup>b)</sup>	43	326	404	7366	171	+40	2.1	0.4
NMC-811#20 <sup>b)</sup>	35.7	327	424	6648	186	+54	2	0.4
NMC-811#22 <sup>ref,b)</sup>	36.5	337	424	7528	206	+44	2.2	0.3

a) All SLP cells were visually inspected in the post-mortem analysis. b) used for SEM/EDX post-mortem analysis. c) from capacity check-up  $CC_{DCH}$  (see Table III). d) Impedance at 4.2 V and  $Im = 0$ . e) Impedance at 4.2 V and 1 kHz. f) ref. to  $|Z|_{1kHz}$  before and after the short-circuit event. g) after a minimum of five days for relaxation.



**Figure 8.** Normalized heat dissipation  $\left(\frac{Q_{tot}}{\int_0^{tot} E \cdot I dt}\right)$  of ESC tests applied with 0 V (a) and 500 m $\Omega$  (b) condition, LSC tests applied with  $\varnothing$  1 mm needle penetration (c), and ESC tests applied to aged cells (d). The results of NMC-111 cells are shown in a), b), and c) as a benchmark to the NCA and NMC-811 cells. The maxima of the plots a) to d) are summarized in subplot e).

601 J and 541 J, which reveals the same correlation to the capacity as for the NCA cells.

The current plateaus of the NMC-811 cells reveal a slightly shorter duration due to the lower impedance and the lower capacity. A higher current level of plateau III\* appears compared to the NCA cells, which can be ascribed to a cathode effect as the only difference in manufacturing the cells was the cathode. Besides, the SLP cells perform quite similar in terms of plateau and transition zone characteristics for current, terminal voltage, and heat generation rate as well as the total dissipated heat. A marginal tendency of increased heat converted out of the electrical energy appears for the NMC-811 cells compared to the NCA cells, which will be further

analyzed later in this work. In general, the higher the short-circuit intensity, the higher the amount of converted electrical energy during the ESC into thermal energy appears.

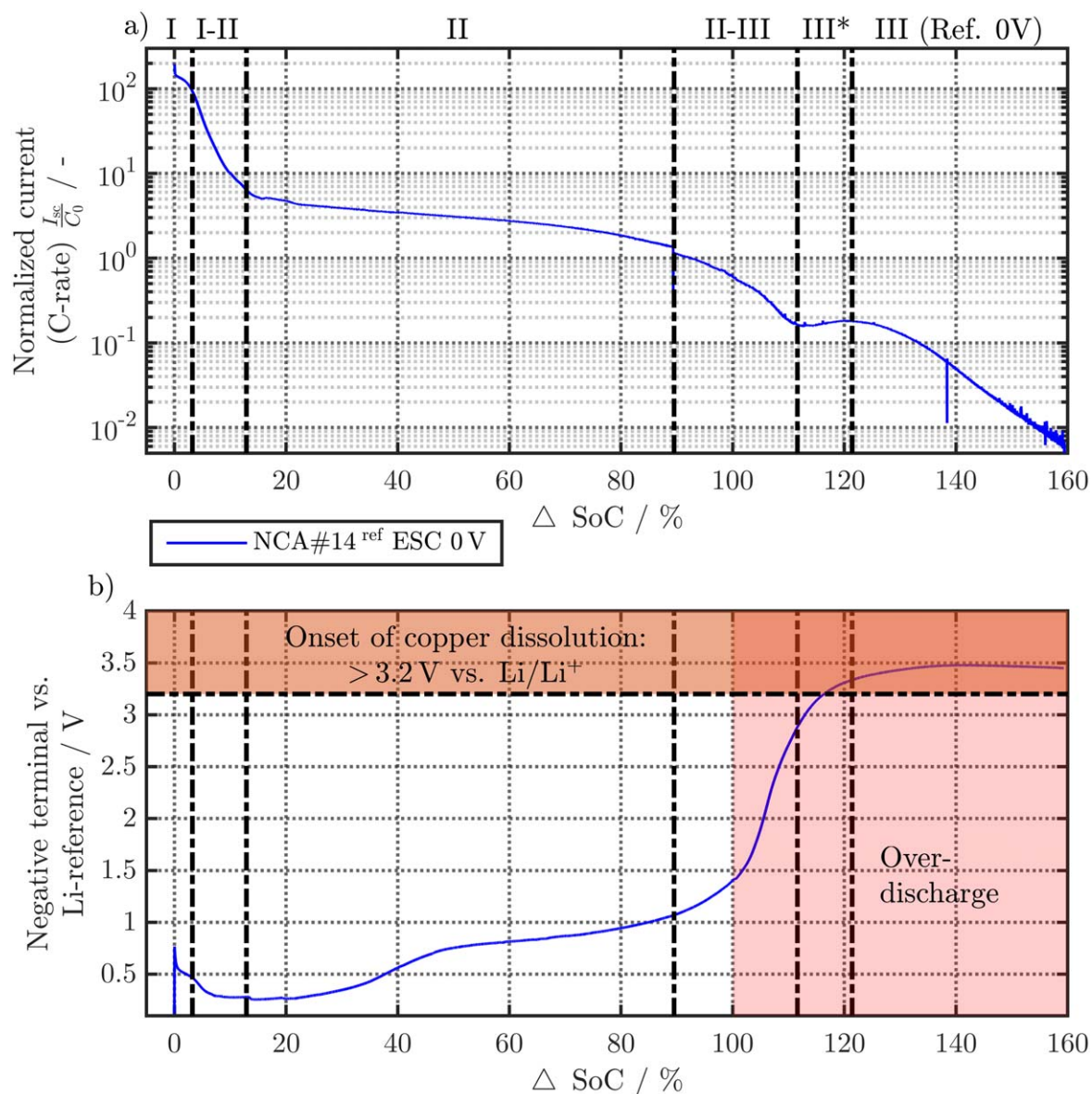
To better compare the NCA and NMC-811 cells during the short-circuit event, the ESC test results of the 0 V and the 500 m $\Omega$  case are shown over the discharged  $\Delta$  SoC in Fig. 5. Regarding the current rate in Fig. 5a and 5b, the discharged capacity reaches the initial capacity  $C_0$  within the II-III transition zone marking the onset of over-discharge. As the anode is limiting the cell's capacity this marks the point when the anode's capacity is exceeded. With ongoing discharge and over-delithiation, anode potentials are vastly increasing most likely triggering copper dissolution from the



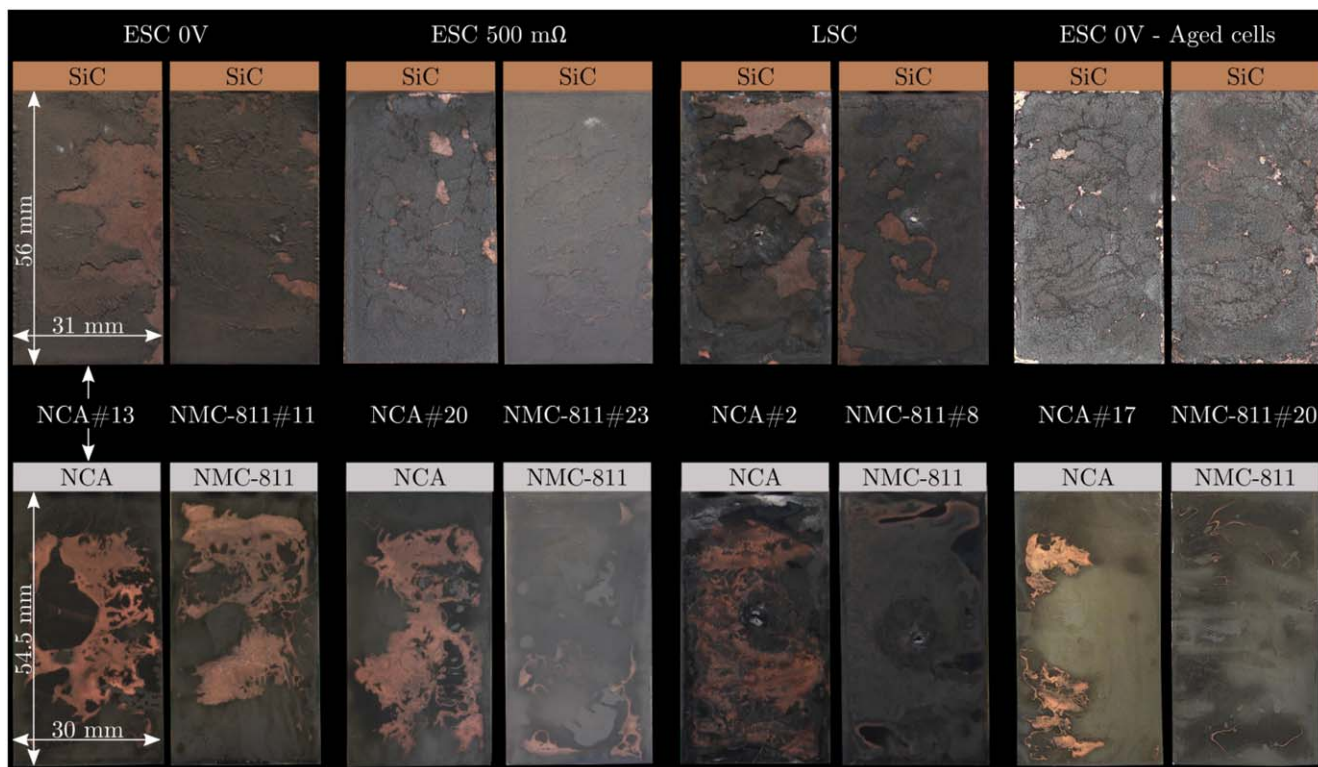
**Table IX. Potentiostatic results of the ESC tests applied to SLP cells with reference electrode.**

Symbol Unit	$C_0^c)$ mAh	$R_{\text{Im}\{Z\}=0,0}^d)$ $\text{m}\Omega$	$ Z _{1\text{kHz},0}^e)$ $\text{m}\Omega$	$R_{\text{ext}}$ $\text{m}\Omega$	$\frac{R_{\text{ext}}}{R_{1\text{kHz},0}}$	$I_{\text{max}}$ mA	C-rate <sub>max</sub> —	$\Delta$ SoC %	$\frac{ Z _{1\text{kHz},\text{sc}}^f)}{ Z _{1\text{kHz},0}}$	$E_{\text{sc,end}}^g)$ V
<b>Cell ID<sup>a)</sup></b>										
NCA#14	38.7	377	530	0 ('0 V')		7530	195	+59	1.7	1.7
NCA#16	45.8	407	554			6868	150	+20	1.5	2.5
NCA#23	44	504	661	50	0.08	4640	105	+32	2.3	0.4
NCA#15	44	302	428	500	1.17	3830	87	+33	1.4	0.6
NMC-811#12	32.6	400	486	0 ('0 V')	0	6730	206	+33	1.7	1.2
NMC-811#13	35.3	385	463			7947	225	+39	2	1.3
NMC-811#15	35.2	322	385			9141	260	+41	1.4	0.2

a) All SLP cells were visually inspected in the post-mortem analysis. b) used for SEM/EDX post-mortem analysis. c) from capacity check-up  $CC_{\text{DCH}}$  (see Table III). d) Impedance at 4.2 V and  $\text{Im}\{Z\} = 0$ . e) Impedance at 4.2 V and 1 kHz. f) ref. to  $|Z|_{1\text{kHz}}$  before and after the short-circuit event. g) after a minimum of five days for relaxation.



**Figure 9.** Test results over  $\Delta$  SoC of normalized current  $\frac{I_{\text{sc}}}{C_0}$  (a) and the measured electrical potential between the negative terminal and the lithium reference electrode during a 0 V ESC test of cell NCA#14. The plateaus and transition zones (I, I-II, II, II-III, III\*, and III) are determined for the current profile. Subplot b) depicts the region of over-discharge (red) and the region of possible copper dissolution (orange) beyond 3.2 V vs Li/Li<sup>+</sup>.



**Figure 10.** Post-mortem analysis showing photographs of chosen NCA (#13, #20, #2, and #17) and NMC-811 (#11, #23, #8, and #20) SLP cells of each applied short-circuit condition as depicted in Fig. 8 (i.e. ESC 0 V, ESC 500 mΩ, LSC, and ESC 0 V applied to aged cells).

negative current collector<sup>4,12</sup> and driving the observed over-discharge of the cell until the end of the short-circuit test. As shown in Table V, the plateaus and transition zones can be correlated to  $\Delta$  SoC as well and at the end of the transition II-III, all cells reach an over-discharged state (i.e.  $\Delta$  SoC > 100%).

Regarding the increase of  $\Delta$  SoC during plateau III\* and the aforementioned correlation to the oversized cathode, the slightly increased gain of approximately +6% appears in both ESC cases for the NMC-811 cells. The earlier onset of transition II-III can be explained by the overall lower capacity of the NMC-811 cells after formation (see Table IV), the higher cathode areal capacity (see Table II), and the slightly increased overdimensioning of the cathode in the over-discharge region of the NMC-811 compared to the NCA cells. This is due to an earlier discharge of the NMC-811 cells caused by the earlier anode limitation and the increased  $\Delta$  SoC levels during plateau III\* due to the larger NMC-811 cathode capacity.

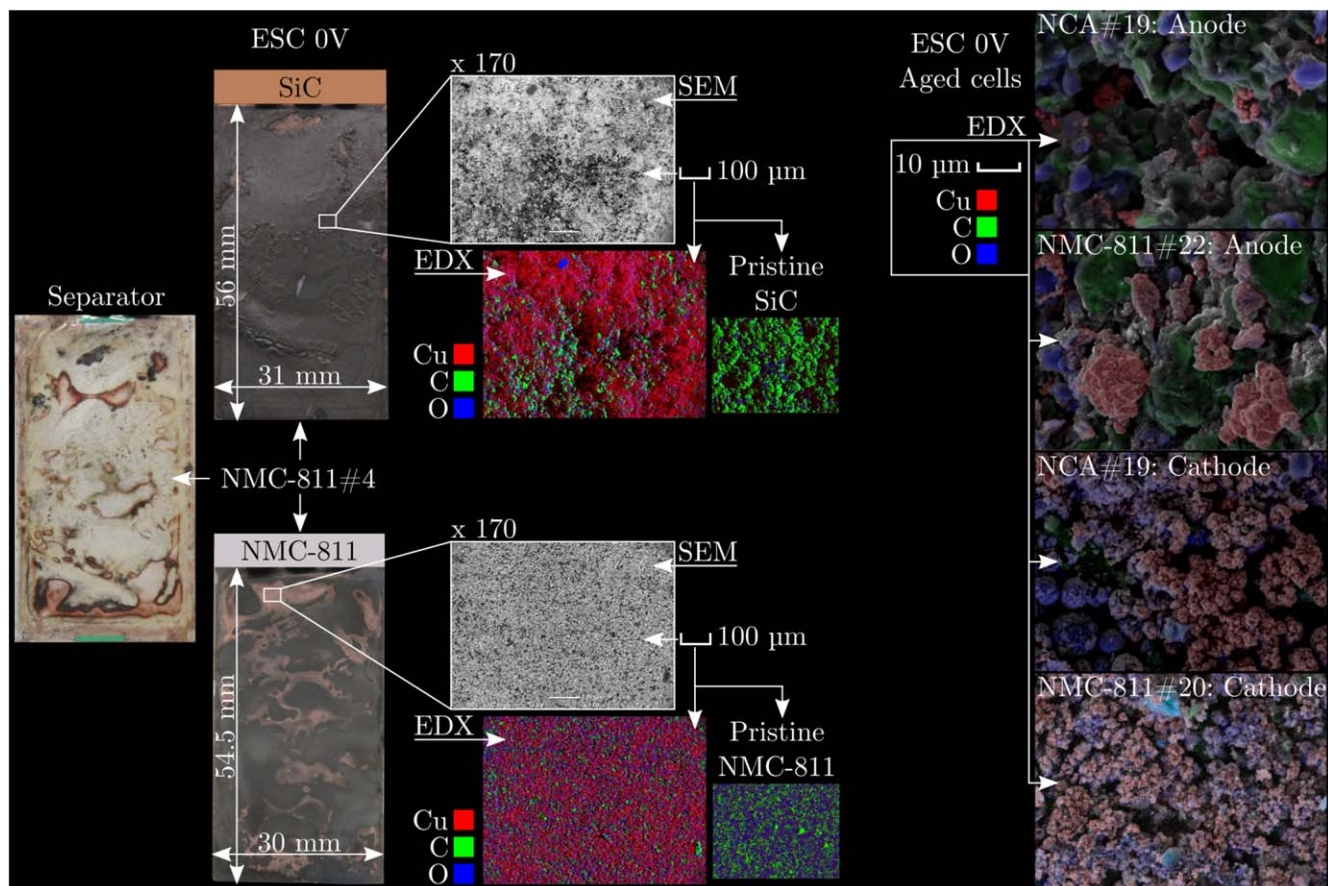
Regarding the heat generation rate in Fig. 5c and 5d, the plateau III\* of the current leads to the observed heat rate plateau, which is entirely occurring during over-discharge. The high current levels in the beginning lead to the observed steep increase of the dissipated heat shown in Fig. 5e and 5f, which attenuates after the I-II transition and increases during plateau II until the onset of over-discharge. During over-discharge, the SLP cells still convert a significant amount of electrical energy into thermal heat, which sums up to 19% of the total dissipated heat for both NMC-811 cells. In case of the NCA cells, 16% and 29% of the total heat result from the 0 V and the 500 mΩ case, where the slightly increased amount of heat in the higher ohmic case is caused by the higher over-discharge of the tested NCA#20 cell. The NCA#20 cell revealed the lowest ESC intensity with an initial current maximum of 85C, which caused prolonged current plateaus until the end of plateau II and thus increased dissipated heat as seen in Fig. 5f. Considerable amounts of heat emerge from the conversion of electrical energy after exceeding the fully discharged state of the NCA and NMC-811 cells (i.e.  $\Delta$  SoC > 100%), which must be taken into account in terms of safety

risks of LIBs. A profound comparison of the former standard graphite/NMC-111 cells from our previous works<sup>3,4,12</sup> to the silicon-graphite/nickel-rich NCA and NMC-811 cells exceeds the scope of this work and is provided in the supplementary material.

**LSC applied to NCA and NMC-811 SLP cells.**—Six LSC tests were chosen to analyze the short-circuit behavior of NCA and NMC-811 cells. The characteristics of capacity and impedance of the tested cells are summarized in Table VI. In the following, the LSC test results of the cells NCA#2 and NMC-811#8 are presented in Fig. 6 and correlated to comparable ESC cases of this work to evaluate the intensity of the short-circuit event induced by needle penetration.

Referring to Fig. 4c, the terminal voltage  $E_{sc}$  during the ESC cases of both NCA and NMC-811 cells appear with marginal differences until plateau III\*, as discussed before. This is why Fig. 6a shows only the ESC of NCA cells as a reference for the 50 mΩ, 250 mΩ, and 500 mΩ conditions. A marginal increase of the terminal voltage appears for both LSC cases (i.e. NCA#2 and NMC-811#8) right after the needle penetration until 1 s of the short-circuit event, which is ascribed to the formation and alteration of the contact condition<sup>7,12</sup> between the needle and the penetrated electrode stack. In this matter, Fig. 6d shows the terminal voltage  $E_{sc}$  and the measured electrical potential between the cell's negative tab and the electrically-contacted needle  $\Phi_{sc}$  (see Fig. 2, bottom left). Until the very first second of the LSC event, the measured needle potential indicates increased noise and short-term local minima (see NCA#2 until  $\approx$  0.01 s), which also indicates contact alteration.<sup>7,12</sup> After 1 s, plateau I is passed and the terminal and needle potential profiles show similar short-circuit characteristics at different intensities, as seen for ESC cases. For example, the LSC intensity of the NCA#2 cell can be evaluated in between the 50 mΩ and 250 mΩ ESC case during plateau I (i.e. until 1 s) and a higher ohmic behavior close to the 250 mΩ case appears until 100 s. Afterwards, the profile adapts to the 500 mΩ case and even beyond until the end of the LSC test. For the NMC-811#8 cell, similar characteristics can be observed showing an earlier voltage drop around 450 s due to the faster





**Figure 11.** Post-mortem analysis showing SEM and EDX analysis (JCM-600, JEOL Ltd., Germany) of cell NMC-811#4 after a ESC 0 V test. The dismantled anode (upper left), separator (left, depicted relative to the anode position), and cathode (lower left) are shown as photographs and indicate the extraction of the samples for the SEM and EDX tests. In the middle, the SEM images (white frame, magnification level of 170) are shown together with the applied EDX analysis, where the EDX results of the pristine materials are shown as a reference. On the right side, EDX analysis (JEOL JSM-IT200, JEOL Ltd.) is applied to 2000 times magnified positions at the anode and cathode surfaces of aged cells (NCA#19, NMC-811#20, and NMC-811#22) after the ESC 0 V test and highlights depositions of copper.

discharge caused by the lower cell capacity. Considering the slightly higher current rates during plateau I until transition zone I-II of the NMC-811 cells compared to the NCA cells (see Fig. 4), most likely the current flow in the penetration region of the NMC-811#8 is higher compared to the NCA cells as the interpretation of the terminal voltage indicates, even if the terminal voltage profiles are quite similar. This is correlated with the lower capacity<sup>3</sup> and the lower impedance of the NMC-811 cells compared to the NCA cells, as discussed before.

No current flow measurement during the LSC tests is available, as the analysis of the electrical potentials is affected by polarization effects along with the current collectors, through the thickness of the electrode stack, and the alteration of the contact condition in the penetration spot,<sup>7,12</sup> and the current flow through the electrically contacted needle. The heat generation rate is an alternative to interpret the intensity of the short-circuit event, correlating the LSC to the ESC cases. Regarding the heat generation rate in Fig. 6b and c), the LSC of NMC-811#8 indicates a quite similar profile as the NMC-811#11 ESC 0 V case. The LSC of NCA#2 resembles the NCA#11 250 mΩ case in the beginning and shows again the higher ohmic behavior in the following zones. As a result, the interpretation of the measured electrical potentials is affected by in- and through-plane polarization effects and alteration of the contact condition, which is why a correction as proposed in our previous work with a multiphysics simulation tool<sup>12</sup> is crucial for a correct interpretation of the LSC intensity. Alternatively, the intensity of the LSC events can be estimated by correlating the heat generation rate to ESC cases.

**Effect of aging on ESC characteristics for NCA and NMC-811 cells.**—Two NCA and two NMC-811 SLP cells with and without the reference electrode setup underwent a cyclic aging procedure resulting in SoH levels below 80%. Then, the aged cells were tested under a 0 V ESC condition due to the higher reproducibility of ESCs compared to LSCs. The focus of the aging study was not the analysis of the specific aging behavior of the NCA and NMC-811 cells, which would have required a larger number of tested cells. The aging study was designed to emulate short-circuits occurring in aged cells, which are characterized by a certain capacity loss (i.e. SoH level below 80%) and an increased cell impedance. The results of the cyclic aging procedure are summarized in Table VII.

Around 1000 equivalent full cycles (Efc) appear for the NCA cells, whereas no distinct difference in the overall aging behavior could be observed between the SLP cell with (NCA#17) and without (NCA#19) a reference electrode. The respective levels of SoH accounted for 74.8% and 75.3% accompanied by an impedance (i.e. at 1 kHz) increase of +22% and +17%. In case of the aged NMC-811 cells, the SLP cell with the reference electrode setup showed a significantly lower number of Efc (i.e. NMC-811#22 with 793 Efc) compared to the standard SLP cell (NMC-811#20 with 1454 Efc). This is most likely caused by the self-built cell manufacturing process. Nevertheless, at 76.9% and 78.1% SoH similar impedance increases around +12% and +11% appear for the NMC-811#20 and the NMC-811#22 cell. The increased impedance and the decreased capacity are expected to have a significant influence on the short-circuit intensity, which is analyzed with the results of the applied 0 V ESC tests.

**Table X. Formation and initialization test protocols for NCA and NMC-811 SLP cells.**

Formation <sup>s)</sup>			Chamber Temperature
Repetition	Sequence <sup>a)</sup>	Feature	
2×	CC <sub>CH</sub> -CV-R-CC <sub>DCH</sub> -R	CC: 5.7 mA, 3 V–4.2 V CV: <1.1 mA R: 30 min	25 °C
4×	CC <sub>CH</sub> -CV-R-CC <sub>DCH</sub> -R	CC: 11 mA, 3 V–4.2 V CV: <1.1 mA R: 30 min	
1×	CC <sub>CH</sub> -CV-R-CC <sub>DCH</sub> -R	CC: 57 mA, 3 V–4.2 V CV: <1.1 mA R: 30 min	
1×	CC <sub>CH</sub> -CV-R	CC: 11 mA, 3.75 V CV: <1.1 mA R: 30 min	
EIS with 5 m V excitation voltage from 10 mHz to 200 kHz <sup>b)</sup>			
<b>Optional OCV<sup>c)</sup>, EIS characterization protocol<sup>d)</sup></b>			
<b>Storing until scheduled ESC or LSC test at 5 °C</b>			
<b>Initial cycles</b>			
Thermal equalization for 12 hat 25 °C			
2×	CC <sub>CH</sub> -CV-R-CC <sub>DCH</sub> -R	CC: 0.1C, 3 V–4.2 V CV: <0.01C R: 15 min	25 °C
8×	CH-CV-R-CC <sub>DCH</sub> -CV-R	CC: 0.5C, 3 V–4.2 V CV: <±0.01C R: 15 min	
1×	CC <sub>CH</sub> -R	CC: 0.5C to 50% SoC R: 30 min	
1×	P <sub>CH</sub> -R-P <sub>DCH</sub> -R	P: 0.3C, 1C and 2C for 10 s R: 10 min	

a) CC<sub>CH</sub> constant current charge CC<sub>DCH</sub> constant current discharge CV constant voltage R rest/relaxation period P<sub>CH</sub> charge pulse current P<sub>DCH</sub> discharge pulse current s) Supplier's recommendation. b) 8 points per decade and 3 measurements per frequency. c) OCV for chosen NCA and NMC-811 cells. d) EIS characterization for chosen NCA and NMC-811 cells at 14 points between 0% and 100% SoC with 5 m V excitation voltage from 10 mHz to 200 kHz and 8 points per decade and 3 measurements per frequency.

Figure 7 shows the normalized current rate (a,b), the heat generation rate (c,d), and the dissipated heat (e,f) over the withdrawn  $\Delta$  SoC in reference to the initial capacity  $C_0$  of the fresh cells. Lower initial current rates (see Table VIII) of at least –16% appear for the aged NCA cells (#17, #19) compared to the non-aged NCA cell (#13) at the very beginning of the 0 V ESC test, which corresponds to impedance differences as expected. Regarding the current rate profile in Fig. 7a, shorter plateau zones I, II and III\* appear due to the lower capacity of the aged NCA cells. Nevertheless, the over-discharge of the aged SLP cells reaches similar levels as the non-aged ones (see Table IV and Fig. 7, NCA#13 and NMC-811#11). Significant levels of over-discharge appear for aged SLP cells, which are nearly equal to the levels of non-aged SLP cells. As a result, also aged cells with SoH levels below 80% can be over-discharged close to levels of non-aged SLP cells, albeit an overall lower intensity of the short-circuit due to shorter and lower current plateaus can be observed.

Regarding the heat generation rate and the total dissipated heat in Fig. 7c and 7e, the heat rate follows the shorter and lower trends of the current profiles and the overall dissipated heat of 109 J is around 12% lower than for the non-aged cell NCA#13. The amount of dissipated heat converted from the electrical energy significantly decreases by -12% for the NCA cell. Unfortunately, in case of cell NCA#19 no heat generation rate and dissipated heat could be measured due to malfunction of the measurement equipment.

In general, similar results appear for the comparison of the NMC-811 cells shown in Figs. 7b, 7d, and 7f. Interestingly, cell NMC-811#22 shows only a 6% lower level of dissipated heat compared to the non-aged reference (NMC-811#11) and higher current and heat generation plateaus compared to cell NMC-811#20. Despite the

faster degradation of cell NMC-811#22 resulting from the lower number of EfCs, the short-circuit intensity was not affected in the same way as a more intensified short-circuit with higher current rates and heat dissipation appeared during the ESC test.

**Overall comparison of ESC and LSC tests results for the NCA, NMC-811, and NMC-111 cells.**—To compare the different short-circuit tests presented in this work, an estimate for the conversion of electrical energy into thermal energy<sup>3</sup> is calculated via referencing the total heat dissipation  $Q_{tot}$  during the short-circuit test to the electrical power ( $E \cdot I$ ) integrated over time from the last initial cycle sequence at 0.5C (see Table X, from 100% to 0% SoC). The results are the calculated normalized heat dissipation, as shown in Fig. 8 for the ESC tests applied with 0 V (a) and 500 mΩ (b) condition, the LSC tests applied with  $\varnothing$  1 mm needle penetration (c), and the 0 V ESC tests applied to aged cells (d). The NMC-111 cells are shown for the non-aged ESC and LSC tests from our previous work<sup>12</sup> as a benchmark.

Overall, a decreasing trend for the maxima and the slope over time appears regarding Fig. 8a to 8d beginning with the most intensive short-circuits at 0 V (a) to the lowest (d) as seen for the aged SLP cells. Again, the NMC-111 cells reveal a higher conversion rate of electrical into thermal energy for the ESC cases as discussed before and show a significant share in the over-discharge region (i.e. >100%). Regarding Fig. 8d, the aged SLP cells show both a significantly lower conversion into thermal energy, which is in the range of the initial electrical energy of the SLP cells. Figure 8e shows the maxima of the normalized heat rates and again, the decreasing trend with lower intensity of the short-circuit event appears. The decrease in converted thermal energy as shown in



Table XI. Abbreviations.

CC <sub>CH</sub>	constant current charge
CC <sub>DCH</sub>	constant current discharge
CV	constant voltage
DMC	dimethyl carbonate
DVA	differential voltage analysis
EC	ethylene carbonate
EMC	ethyl methyl carbonate
ESC	external short-circuit
G	graphite
LiPF <sub>6</sub>	lithium hexafluorophosphate
LCO	lithium cobalt oxide
LSC	local short-circuit
LMO	lithium manganese oxide
LNCO	lithium nickel-cobalt oxide
NCA	SiC/NCA electrodes in SLP cells with Li <sub>y</sub> (Ni <sub>0.8</sub> Co <sub>0.15</sub> Al <sub>0.05</sub> )O <sub>2</sub> as cathode material
NMC	lithium nickel-manganese-cobalt oxide
NMC-111	G/NMC-111 electrodes in SLP cells with Li <sub>y</sub> (Ni <sub>0.33</sub> Mn <sub>0.33</sub> Co <sub>0.33</sub> )O <sub>2</sub> as cathode material
NMC-811	SiC/NMC-811 electrodes in SLP cells Li <sub>y</sub> (Ni <sub>0.8</sub> Mn <sub>0.1</sub> Co <sub>0.1</sub> )O <sub>2</sub> as cathode material
OCV	open circuit voltage
P <sub>CH</sub>	charge pulse current
P <sub>DCH</sub>	discharge pulse current
R	rest/relaxation period
SiC	graphite host lattice containing silicon
SLP	single-coated, single-layered pouch (cells)
VC	vinyl carbonate

Fig. 8e for the ESC at 0 V applied to non-aged and aged cells accounts for  $-30\%$  and  $-20\%$  for the NCA and the NMC-811 cells. In case of the NMC-111 cells, the decrease between the ESC at 0 V and the LSC accounts for  $-27\%$ .

As a result, the intensity of the different short-circuits can be estimated via the normalized heat rate and thus the ESC at 0 V is the most intensive short-circuit investigated in this work, followed by the ESC at 500 mΩ, the LSC with  $\varnothing$  1 mm needle penetration, and the ESC at 0 V applied to aged cells. Comparing the NCA and NMC-811 cells to each other, a slight tendency of increased thermal energy appears for the NMC-811 cells independently on the applied short-circuit test.

**ESC applied to NCA and NMC-811 SLP cells with lithium-reference electrode.**—Exemplary OCV and impedance test results between standard and modified SLP cells with reference electrodes are shown in the supplementary part of this work. In general, inserting the reference electrodes into NCA and NMC-811 cells revealed negligible differences under normal test conditions. During the ESC tests, similarly, no significant influence of the reference electrode setup could be observed toward the cell's short-circuit characteristics of discharge current, terminal voltage, and heat generation rate.

Table IX summarizes the ESC tests of the modified NCA and NMC-811 cells. Regarding cell NCA#14, a 0 V ESC results in a maximum C-rate of 195C ( $\cong$  7.53 A) in the very beginning and leading to an over-discharge of  $+59\%$   $\Delta$  SoC. The profile of the short-circuit current is exemplarily shown in Fig. 9a for the cell NCA#14. Plateau I lasts approximately until  $3.2\%$   $\Delta$  SoC, the transition zone I-II until  $12.9\%$   $\Delta$  SoC, and the second current plateau finishes at around  $90\%$   $\Delta$  SoC. The following II-III transition zone lasts approximately until  $112\%$   $\Delta$  SoC and plateau III\* with a local current maximum around 0.2C ends at around  $121\%$   $\Delta$  SoC. These results are well in line with the findings of the SLP cell without a reference electrode setup from Table V.

The measurement of a local electrical potential at the anode is the benefit of having a reference electrode setup, which can be used to better understand the processes during the short-circuit. The signal is measured between the cell's negative tab and the incorporated

lithium metal reference electrode placed next to the electrode stack, as already described and depicted in Fig. 1 and Fig. 2.

However, the measured lithium metal reference signal (see Fig. 9) is distorted by several polarization effects, which occur along the in- and the through-plane direction of the SLP cell setup<sup>24</sup> and result in non-negligible over-voltages. In-plane voltage losses occur dominantly along the width of the negative current collector (see Fig. 1) due to the counter-tab design<sup>3</sup> of the SLP cells. In our previous work<sup>12</sup> for the NMC-111 cells, the in-plane voltage loss was estimated to be up to 32 mV using multi-dimensional multi-physics simulation tools. Through-plane voltage losses can be studied following the work of Nyman et al.<sup>29</sup> into polarization effects of electrolyte diffusion, particle diffusion, ohmic losses in the electrolyte and solid electrode phase, and the reaction kinetics at the solid-liquid interface in the electrode domains. It can be used for the analysis of short-circuit events via high-current modified electrochemical simulation tools and enable the aforementioned categorization into plateau and transition zones I to III.<sup>4</sup> As shown in the work of Rheinfeld et al.,<sup>4</sup> the through-plane polarization especially at the beginning of an ESC 0 V for a NMC-111 cell is estimated to be in the magnitude of volts and rapidly ( $<100$  s) decreases down to the range of milli-volts and significantly increases to the range of volts again, when the anode is close to full-delithiation and the over-discharge of the cell initiates. As seen in the comparison of NCA and NMC-811 cells with the NMC-111 cells in the sections before, most likely similar polarization effects despite the anode-limiting effect (i.e. III\* zone) appear and justify the comparison here. The measured signal presented in this work incorporates the in- and through-plane polarization effects beside the pathway from the electrode stack to the position of the lithium reference through the electrolyte. In this work, the measured electrical signal is used to estimate the anode polarization incorporating the aforementioned influences on the measurement signal.

Interestingly, the measured signal resembles the simulated potential drop between the solid and liquid phase at the position of the negative current collector at significantly lower values of the potentials (i.e. approximately a factor of 0.5) which was simulated in our previous work<sup>2</sup> to estimate the possible onset of copper dissolution. Note, that the measured signal is not meant to be a

precise representation of the anode's potential or the potential drop between the solid and liquid phase, but most likely indicates how the potential states in the anode may evolve during a short-circuit event.

The measured potential profile is shown in Fig. 9b). At the very beginning of the short-circuit, the signal increases instantaneously from approximately 120 mV (i.e. anode equilibrium potential at 100% SoC) to 770 mV. During plateau I, most likely the measured potential increase is caused by the anode's deintercalation kinetics and polarization effects of the electrolyte in the pore of the anode.<sup>4</sup> Until the end of plateau I, the signal decreases to 470 mV and shows a further decreasing trend until the end of transition I-II, which is most likely related to particle depletion in the anode and an overall reduction of the anode polarization.<sup>4</sup> During plateau II at approximately 20%  $\Delta$  SoC, the signal starts to increase until 51%  $\Delta$  SoC, where a second plateau is reached, which significantly increases after passing 100%  $\Delta$  SoC. Here, a slight increase compared to the rather constant simulated profile<sup>4</sup> appears, which can be caused by the ongoing delithiation of the anode and related equilibrium potential of the anode and the earlier onset of full-delithiation of the limiting anode regarding the balancing of the cell while simultaneously electrolyte depletion could occur. At this point, simulation studies especially due to the steeper flank caused by the silicon can investigate more the observed potential increase, which could be the content of future research work.

The onset of over-discharge ( $>100\%$   $\Delta$  SoC) is correlated to the capacity limitation of the anode and further delithiation leads to an increase of the anode's potential vs Li/Li<sup>+</sup> and the over-voltage mainly caused by the ongoing deintercalation process.<sup>4</sup> During the plateaus III\* and III, the signal increases beyond 3.2 V, which was correlated in other works<sup>30</sup> to the onset of copper dissolution. As a result, the depicted regions of over-discharge (red) and copper dissolution (orange) of Fig. 9 indicate the very probable onset of copper dissolution from the negative current collector, where especially their overlap indicates copper dissolution reaction during the zones III\* and III. As the measured signal is restricted to the position of the reference electrode, its local variance across the active electrode area cannot be estimated herein, and more or less utilized regions could reveal an earlier or later onset.

In extension to our previous works,<sup>3,4,12</sup> a local potential state could be measured, which can be used to estimate the anode's polarization during the short-circuit via an electrical potential signal. Copper dissolution during the over-discharge of the anode-limited NCA and NMC-811 cells could be monitored using this signal during the analyzed ESC tests.

**Post-mortem analysis.**—The post-mortem analysis is based on visual inspection and SEM/EDX analysis of the disassembled cells, electrodes, and separators after the short-circuit events. Figure 10 shows photographs of anodes and cathodes from disassembled NCA and NMC-811 cells, which were selected from the different short-circuit cases, as discussed in Fig. 8. Obviously, all cathode samples reveal significant copper plating at the surface for every investigated short-circuit case. Compared to our previous results with NMC-111 cells,<sup>3,12</sup> the copper deposits appear more clearly due to the anode-limiting balancing effect and at comparable over-discharge levels. This is why more copper is most likely dissolved from the negative current collector and plates partly the cathode surface. Moreover, a part of the dissolved copper plates at the surface of the anode, as can be seen at the surface of the anode especially for the high-intensive 0 V ESC cases.

Considering the molar mass of copper ( $M_{Cu} = 63.5 \text{ g mol}^{-1}$ )<sup>3</sup> and the dimensions of the copper current collector at the active electrode area ( $31 \text{ mm} \times 56 \text{ mm} \times 14 \text{ }\mu\text{m}$ ), the maximum amount of copper to dissolve is calculated as 217.8 mg with the density of copper ( $\rho_{Cu} = 8.96 \text{ g cm}^{-3}$ ). Applying Faraday's constant ( $96485.3 \text{ As mol}^{-1}$ ), with the entire copper current collector dissolution, 184 mAh could be extracted, if copper was dissolved into Cu<sup>2+</sup> ions.<sup>2</sup> According to Flügel et al.,<sup>31</sup> the current collector copper is dissolved during 0 V discharge at long discharge times in the range of 100 h to

1000 h into Cu<sup>+</sup> ions, which would result in 92 mAh at total copper current dissolution.

To estimate the amount of possibly dissolved copper, exemplary the amount of over-discharge for cell NCA#13 (16.3 mAh, see Table IV) and NMC-811#11 (18.6 mAh, see Table IV) during the ESC 0 V case are calculated. For the NCA#13 and the NMC-811#11 cells, this would result in 19 mg (Cu<sup>2+</sup>) or 39 mg (Cu<sup>+</sup>) and 22 mg (Cu<sup>2+</sup>) or 44 mg (Cu<sup>+</sup>) of copper. As a result, approximately 9% (Cu<sup>2+</sup>) or 18% (Cu<sup>+</sup>) and 10% (Cu<sup>2+</sup>) or 20% (Cu<sup>+</sup>) of the copper current collector were most likely dissolved for the cell NCA#13 and NMC-811#11.

SEM images of anode and cathode samples before and after the short-circuit indicate high mechanical degradation as delaminations, crackings of the coating layer and single particles, and holes in the coating layer appear for the anode and severe surface deposition layers as well as particle cracking for the cathode. This is similar to our previous work.<sup>3</sup>

Interestingly, indications of deposited copper can be found at the separator, as shown in Fig. 11, which fell off from the surfaces of anode and cathode during the SLP cell opening process. The EDX analysis of the NMC-811#4 indicates significant amounts of copper both at the anode and the cathode surface, as seen in Fig. 11. Exemplary, magnifications of anode and cathode surfaces from selected aged SLP cells are investigated with EDX to highlight the deposition of copper, as shown on the right side of Fig. 11. Following our previous work,<sup>12</sup> copper can be indicated most likely also through the coating thicknesses of the anode, as the EDX analysis of the anode from cell NCA#19 suggests (see Fig. 11 upper right side) with indications of copper not only at the surface, but also through the thickness of the coating.

A significant increase of copper plating due to anode-limited balancing of the NCA and NMC-811 cells appears obviously at the surface of the SLP cells, which could be justified with EDX analysis. Up to 20% or 10% of the negative current collector seems to be dissolved during the most intensive ESC 0 V test, assuming either Cu<sup>+</sup> or Cu<sup>2+</sup> dissolution.

## Conclusions

In total 35 short-circuit tests were applied to custom-built single-layered pouch-type SiC/NCA and SiC/NMC-811 cells in a quasi-isothermal calorimetric test bench. The calibrated test bench allowed for keeping the cell's temperature almost constant ( $\Delta T < 1 \text{ K}$ ) and thus enabled the investigation of the cell's short-circuit behavior without any thermal side reactions such as thermal runaway. In contrast to our previous works<sup>3,4,12</sup> dealing with former standard graphite/NMC-111 LIBs, we focus here on silicon-graphite/nickel-rich cell chemistries, which are currently the state-of-the-art of high-energy LIBs.<sup>24</sup> 18 ESC tests were applied with four different external conditions (0 V, 50 m $\Omega$ , 250 m $\Omega$ , and 500 m $\Omega$ ) to study the variance of the short-circuit's intensity via analyzing the normalized discharge current flow, the terminal voltage, and the heat generation rate, as well as the overall dissipated heat. Six LSC tests were applied with needle penetration ( $\varnothing 1 \text{ mm}$ ). The needle potential vs the negative tab could be used to alternatively estimate the short-circuit intensity. Cyclic aging was applied to four SLP cells to study its effect on the ESC behavior applied with a 0 V condition. Beside the standard cell design, seven SLP cells incorporating a reference electrode setup were tested under ESC conditions, where the lithium reference was used to estimate and analyze the anode's potential state during the short-circuit event.

The higher the external resistance, the lower the short-circuit intensity resulting in a lower initial current plateau (i.e. plateau I) and a longer duration until the first transition zone I-II. Overall, the lower impedances and capacities of the NMC-811 compared to the NCA cells result in the observed higher short-circuit intensity. The anode-limited electrode balancing of both cell chemistries leads most likely to the observed third current plateau III\*, which is missing for cathode-limited cells from our previous work.<sup>3,4,12</sup> In

general, the short-circuit behavior of the silicon-graphite/nickel-rich cells is quite similar to the graphite/NMC-111 cells,<sup>5</sup> where similarly the amount of the total dissipated heat is dominated by the cell capacity. Especially during over-discharge significant amounts of dissipated heat appear, which revealed a share up to 29% in case of the NCA cells and should be taken into account in terms of safety risks for LIBs.

The six applied LSC tests revealed similar results as seen in our previous work,<sup>12</sup> where the short-circuit intensity could be correlated to ESC tests in the range from 0 V to 500 mΩ. In the very beginning of the short-circuit, the LSC tests reveal a rather high intensity close to ESC 0 V cases, whereas during plateau II an alteration to higher-ohmic ESC cases appears. In this matter, the heat generation rate enables and eases the comparison to ESC cases, as no current flow can be measured and the terminal voltage is significantly affected by local electrical potential variances across the active electrode area. The alteration of the intensity of the LSC events is most likely affected by the alteration of the contact condition in the penetration site.<sup>7</sup>

The effect of aging resulting in an increased impedance and lower capacity on the short-circuit behavior is analyzed via first applying cyclic aging until SoH levels below 80% to respectively two NCA and NMC-811 cells. Second, ESC 0 V tests result in the expected lower-ohmic short-circuit characteristics (i.e. lower current rates and shorter duration of the current plateaus). Similarly, the amount of converted electrical energy converted into thermal energy decreased. However, the amount of over-discharge reaches nearly the same levels as non-aged cells, which must be taken into account in terms of safety issues for aged LIBs.

An overall comparison of ESC, LSC, and aged ESC tests for the NMC-111, NCA, and NMC-811 cells suggest a decreasing short-circuit intensity for all tested SLP cells resulting in the maximum to be the ESC 0 V case, followed by the ESC 500 mΩ, the LSC case, and the minimum for the aged ESC 0 V tests. In this context, a slight tendency of increased dissipated heat for NMC-811 cells compared to NCA cells appears for the investigated cell chemistries.

The seven ESC tests with NCA and NMC-811 cells incorporating a lithium reference electrode could be used to monitor an electrical potential correlated to the anode's potential, which clearly showed anode-related polarization effects. This is correlated to electrochemical rate-limiting behavior of the cell<sup>3,4</sup> and indicated the onset of over-discharge and copper dissolution during the very last zones of the ESC tests.

The post-mortem analysis revealed a significant increase of copper deposition both on anode and cathode, which occurs significantly more for the investigated anode-limited SLP cells compared to the former investigated cathode-limited SLP cells. Up to 20% of the copper dissolution from the negative current collector could be estimated during a highly intensive ESC 0 V test.

Future work could investigate the observed current plateau III\* via high-current modified electrochemical models<sup>4</sup> to further understand the expected impact of the anode-limited and cathode-over-sized electrode balancing.

### Acknowledgments

This work has received funding from the European Union's Horizon 2020 research and innovation program under the grant 'Electric Vehicle Enhanced Range, Lifetime AndSafety Through INGenious battery management' (EVERLASTING-713771). This work has also partly received funding from the German Federal Ministry of Education and Research (BMBF) under the grants 'ExZellTUM III' (03XP0255) and 'HighSafe II' (03XP0306B). The authors thank the groups of Prof. Hubert A. Gasteiger (Chair of Technical Electrochemistry, Technical University of Munich) and Prof. Dr.-Ing. Michael F. Zäh (Institute for MachineTools and Industrial Management, Technical University of Munich) for the

possibility to carry out SEM and EDX measurements. Moreover, the authors also thank O. Chaouachi and P. Kuntz from University Grenoble Alpes, CEA, France for their help building the NCA and NMC-811 SLP cells.

### Appendix

#### ORCID

J. Sturm  <https://orcid.org/0000-0001-8876-9989>  
 S. Friedrich  <https://orcid.org/0000-0003-1772-8076>  
 D. Buzon  <https://orcid.org/0000-0002-6292-1628>  
 A. Rheinfeld  <https://orcid.org/0000-0003-0995-7266>  
 Jossen A.  <https://orcid.org/0000-0003-0964-1405>

### References

- R. Xiong, S. Ma, H. Li, F. Sun, and J. Li, "Toward a Safer Battery Management System: A Critical Review on Diagnosis and Prognosis of Battery Short Circuit." *iScience*, **23**, 101010 (2020).
- A. Rheinfeld, "Performance and Safety of Lithium-Ion Electrodes and Cells: Modeling, Simulation, and Validation at Elevated Temperatures and Currents." *Ph. D. thesis*, Technical University of Munich (2019).
- A. Rheinfeld, A. Noel, J. Wilhelm, A. Kriston, A. Pfrang, and A. Jossen, "Quasi-Isothermal External Short Circuit Tests Applied to Lithium-Ion Cells: Part I. Measurements." *J. Electrochem. Soc.*, **165**, A3427 (2018).
- A. Rheinfeld, J. Sturm, A. Noel, J. Wilhelm, A. Kriston, A. Pfrang, and A. Jossen, "Quasi-Isothermal External Short Circuit Tests Applied to Lithium-Ion Cells: Part II. Modeling and Simulation." *J. Electrochem. Soc.*, **166**, A151 (2019).
- A. Rheinfeld, J. Sturm, A. Frank, S. Kosch, S. V. Erhard, and A. Jossen, "Impact of Cell Size and Format on External Short Circuit Behavior of Lithium-Ion Cells at Varying Cooling Conditions: Modeling and Simulation." *J. Electrochem. Soc.*, **167**, 013511 (2020).
- A. Kriston, A. Pfrang, H. Döring, B. Fritsch, V. Ruiz, I. Adanoui, T. Kosmidou, J. Ungeheuer, and L. Boon-Brett, "External short circuit performance of Graphite-LiNi1/3Co1/3Mn1/3O2 and Graphite-LiNi0.8Co0.15Al0.05O2 cells at different external resistances." *Journal of Power Sources*, **361**, 170 (2017).
- S. Santhanagopalan, P. Ramadass, and J. Zhang, "Analysis of internal short-circuit in a lithium ion cell." *Journal of Power Sources*, **194**, 550 (2009).
- J. Zhu, M. M. Koch, J. Lian, W. Li, and T. Wierzbicki, "Mechanical Deformation of Lithium-Ion Pouch Cells under In-Plane Loads Part I: Experimental Investigation." *J. Electrochem. Soc.*, **167**, 090533 (2020).
- M. Zhang, J. Du, L. Liu, A. Stefanopoulou, J. Siegel, L. Lu, X. He, X. Xie, and M. Ouyang, "Internal Short Circuit Trigger Method for Lithium-Ion Battery Based on Shape Memory Alloy." *J. Electrochem. Soc.*, **164**, A3038 (2017).
- D. Patel, J. B. Robinson, S. Ball, D. J. L. Brett, and P. R. Shearing, "Thermal Runaway of a Li-Ion Battery Studied by Combined ARC and Multi-Length Scale X-ray CT." *J. Electrochem. Soc.*, **167**, 090511 (2020).
- E. Wang, H. P. Wu, C. H. Chiu, and P. H. Chou, "The Effect of Battery Separator Properties on Thermal Ramp, Overcharge and Short Circuiting of Rechargeable Li-Ion Batteries." *J. Electrochem. Soc.*, **166**, A125 (2019).
- J. Sturm, A. Rheinfeld, D. Buzon, and A. Jossen, "The Impact of the Locality on Short-Circuit Characteristics: Experimental Analysis and Multiphysics Simulation of External and Local Short-Circuits Applied to Lithium-Ion Batteries." *J. Electrochem. Soc.*, **167**, 090521 (2020).
- J. Diekmann, S. Doose, S. Weber, S. Münch, W. Haselrieder, and A. Kwade, "Development of a New Procedure for Nail Penetration of Lithium-Ion Cells to Obtain Meaningful and Reproducible Results." *J. Electrochem. Soc.*, **167**, 090504 (2020).
- K. C. Chiu, C. H. Lin, S. F. Yeh, Y. H. Lin, and K. C. Chen, "An electrochemical modeling of lithium-ion battery nail penetration." *Journal of Power Sources*, **251**, 254 (2014).
- P. T. Coman, E. C. Darcy, C. T. Veje, and R. E. White, "Modelling Li-Ion Cell Thermal Runaway Triggered by an Internal Short Circuit Device Using an Efficiency Factor and Arrhenius Formulations." *J. Electrochem. Soc.*, **164**, A587 (2017).
- S. Huang, X. Du, M. Richter, J. Ford, G. M. Cavalheiro, Z. Du, R. T. White, and G. Zhang, "Understanding Li-Ion Cell Internal Short Circuit and Thermal Runaway through Small, Slow and In Situ Sensing Nail Penetration." *J. Electrochem. Soc.*, **167**, 090526 (2020).
- M. Chen, Q. Ye, Q. Shi, Q. Cheng, Q. Qie, B. Liao, X. Zhai, H. He, and Y. Yang, "New Insights into Nail Penetration of Li-Ion Batteries: Effects of Heterogeneous Contact Resistance." *Batteries & Supercaps*, **2**, 874 (2019).
- R. Zhao, J. Liu, and J. Gu, "Simulation and experimental study on lithium-ion battery short circuit." *Applied Energy*, **173**, 29 (2016).
- A. Abaza, S. Ferrari, H. K. Wong, C. Lyness, A. Moore, J. Weaving, M. Blanco-Martin, R. Dashwood, and R. Bhagat, "Experimental study of internal and external, short circuits of commercial automotive pouch lithium-ion cells." *Journal of Energy Storage*, **16**, 211 (2018).
- Z. Chen, R. Xiong, J. Lu, and X. Li, "Temperature rise prediction of lithium-ion battery suffering external short circuit for all-climate electric vehicles application." *Applied Energy*, **213**, 375 (2018).

21. T. D. Hatchard, S. Trussler, and J. R. Dahn, "Building a smart nail for penetration tests on Li-ion cells." *Journal of Power Sources*, **247**, 821 (2014).
22. T. Yokoshima, D. Mukoyama, F. Maeda, T. Osaka, K. Takazawa, and S. Egusa, "Operando Analysis of Thermal Runaway in Lithium Ion Battery during Nail-Penetration Test Using an X-ray Inspection System." *J. Electrochem. Soc.*, **166**, A1243 (2019).
23. D. P. Finegan, B. Tjaden, T. M M Heenan, R. Jervis, M. Di Michiel, A. Rack, G. Hinds, D. J. L. Brett, and P. R. Shearing, "Tracking Internal Temperature and Structural Dynamics during Nail Penetration of Lithium-Ion Cells." *J. Electrochem. Soc.*, **164**, A3285 (2017).
24. J. Sturm, A. Frank, A. Rheinfeld, S. V. Erhard, and A. Jossen, "Impact of Electrode and Cell Design on Fast Charging Capabilities of Cylindrical Lithium-Ion Batteries." *J. Electrochem. Soc.*, **167**, 130505 (2020).
25. J. Sturm, A. Rheinfeld, I. Zilberman, F. B. Spingler, S. Kosch, F. Frie, and A. Jossen, "Modeling and simulation of inhomogeneities in a 18 650 nickel-rich, silicon-graphite lithium-ion cell during fast charging." *Journal of Power Sources*, **412**, 204 (2019).
26. X. Fleury, "Corrélation entre dégradation des composants internes et sécurité de fonctionnement des batteries Li-ion." *Ph.D. thesis*, Université Grenoble Alpes (2018).
27. J. Schmalstieg, C. Rahe, M. Ecker, and D. U. Sauer, "Full Cell Parameterization of a High-Power Lithium-Ion Battery for a Physico-Chemical Model: Part I. Physical and Electrochemical Parameters." *J. Electrochem. Soc.*, **165**, A3799 (2018).
28. J. Sturm, F. B. Spingler, B. Rieger, A. Rheinfeld, and A. Jossen, "Non-Destructive Detection of Local Aging in Lithium-Ion Pouch Cells by Multi-Directional Laser Scanning." *J. Electrochem. Soc.*, **164**, A1342 (2017).
29. A. Nyman, T. G. Zavalis, R. Elger, M. Behm, and G. Lindbergh, *A new methodology for evaluating the high-power behavior of a li-ion battery cell ECS Transactions (ECS)*, 253 (2010).
30. L. D. Ellis, J. P. Allen, L. M. Thompson, J. E. Harlow, W. J. Stone, I. G. Hill, and J. R. Dahn, "Understanding and Evaluating the Effects of Gas Consumption in Lithium-Ion Cells." *J. Electrochem. Soc.*, **164**, A3518 (2017).
31. M. Flügel, M. Kasper, C. Pfeifer, M. Wohlfahrt-Mehrens, and T. Waldmann, "Cu Dissolution during Over-Discharge of Li-Ion Cells to 0 V: A Post-Mortem Study." *J. Electrochem. Soc.*, **168**, 020506 (2021).